

Millisecond synthesis of CoS nanoparticles for highly efficient overall water splitting

Yanan Chen^{1,§}, Shaomao Xu^{1,§}, Shuze Zhu^{2,§}, Rohit Jiji Jacob³, Glenn Pastel¹, Yanbin Wang¹, Yiju Li¹, Jiaqi Dai¹, Fengjuan Chen¹, Hua Xie¹, Boyang Liu¹, Yonggang Yao¹, Lourdes G. Salamanca-Riba¹, Michael R. Zachariah³, Teng Li², and Liangbing Hu¹ (✉)

¹ Department of Materials Science and Engineering, University of Maryland, College Park, College Park, Maryland 20742, USA

² Department of Mechanical Engineering, University of Maryland, College Park, College Park, Maryland 20742, USA

³ Department of Chemical and Biomolecular Engineering and Chemistry and Biochemistry, University of Maryland, College Park, College Park, Maryland 20742, USA

[§] Yanan Chen, Shaomao Xu, and Shuze Zhu contributed equally to this work.

© Tsinghua University Press and Springer-Verlag GmbH Germany, part of Springer Nature 2019

Received: 9 December 2018 / **Revised:** 19 January 2019 / **Accepted:** 20 January 2019

ABSTRACT

High performance and low-cost electrocatalysts for overall water splitting, i.e., catalyzing hydrogen and oxygen evolution reactions with the same material, are of great importance for large-scale, renewable energy conversion processes. Here, we report an ultrafast (~ 7 ms) synthesis technique for transition metal chalcogenide nanoparticles assisted by high temperature treatment. As a proof of concept, we demonstrate that cobalt sulfide (~ 20 nm in diameter)/few-layer graphene (~ 2 nm in thickness) core-shell nanoparticles embedded in RGO nanosheets exhibit remarkable bifunctional electrocatalytic activity and stability for overall water splitting, which is comparable to commercial 40 wt.% platinum/carbon (Pt/C) electrocatalysts. After 60 h of continuous operation, 10 mA·cm⁻² water splitting current density can still be achieved at a low potential of ~ 1.77 V without any activity decay, which is among the most active for non-noble material based electrocatalysts. The presented study provides prospects in synthesizing highly efficient bifunctional electrocatalysts for large-scale energy conversion application via a simple yet efficient technique.

KEYWORDS

ultrafast, high temperature synthesis, graphene, water splitting

1 Introduction

Due to the ever-rising environmental pollution and the increasing consumption of fossil fuels, green and sustainable energy resources are becoming extremely important to meet the growing demand for energy [1]. Scientific studies on developing green and sustainable energies to address the current environmental and energy challenges have attracted significant interest. Among various green energy technologies, electrochemical/photoelectrochemical water splitting is one of the most promising methods for the production of hydrogen [2–6], an ideal form of green energy. The catalyst is the key factor in the water splitting process, where catalytic activity and stability determine the efficiency of the electrochemical reactions including the hydrogen evolution reaction (HER) and oxygen evolution reaction (OER). In recent years, great progress has been achieved in catalyst design for water splitting [7, 8]. At present, the most active and commonly used catalysts for water splitting are platinum (Pt) [9] for HER, and ruthenium (Ru) or iridium (Ir) oxide [10] for OER. However, these noble metal based catalysts are expensive or unstable, which impedes their large-scale applications. Numerous efforts have been devoted to investigating cost-effective alternatives for water splitting to enable large-scale applications [1–13]. For example, a wide range of earth-abundant alternatives [11, 12, 14, 15] such as nanocarbons [16], transition metal alloys [17], transition metal carbides [18, 19], and transition metal dichalcogenides [20–31] are

electroactive for HER. At the same time, alternative materials [32] including nanocarbons [33, 34], transition metal oxides [35, 36] and transition metal layered double hydroxides [37] have shown electrocatalytic activity for OER. However, it is a challenge to find a single bifunctional and stable catalyst for both HER and OER that could be employed in an integrated electrolyser because of the wide range of operating conditions. Such an achievement, however, would simplify the reaction system and lower the cost.

Recently, cobalt chalcogenide-based materials, such as cobalt-sulfide and cobalt-selenide, are emerging as promising low-cost and highly effective catalysts for either HER or OER [38–46]. Nevertheless, reports on using cobalt chalcogenides as a single bifunctional catalyst for water splitting in an integrated electrolyser are rare. In addition, the most common synthesis method for these catalysts are hydrothermal processes in solution, which are time-consuming and hard to adopt in large-scale manufacturing. Alternatively, electrodeposition of cobalt-sulfide for HER has also been employed; however, this method often leads to aggregation of catalyst particles and weak interactions with the substrate, resulting in poor catalytic performance [47]. Furthermore, catalysts synthesized by the aforementioned methods are always directly exposed to electrolytes, which are often strong acidic or basic solutions, thus leading to inevitable corrosion of active material in the electrolyser.

Here we report a rapid 7 millisecond (ms) high temperature approach for synthesizing graphene matrix-stabilized CoS@ few-layer

graphene core-shell electrocatalysts for efficient overall water splitting. The synthesis of CoS@ few-layer graphene core-shell electrocatalysts encapsulated in RGO is schematically presented in Fig. 1. The precursor-laden film was prepared by mixing cobalt acetate, thiourea, and graphene oxide (Fig. 1(a)), followed by pre-annealing in a tube furnace at 673 K. The raw film was then transformed into cobalt-sulfide nanoparticles and RGO nanocomposite by applying a thermal shock at $\sim 2,000$ K with a current pulse (Fig. 1(a) and Fig. S1 in the Electronic Supplementary Material (ESM)). It is found that the cobalt-sulfide nanoparticles are coated by a few-layer graphene shell during the *in-situ* synthesis. The formation mechanism of CoS@ few-layer graphene is proposed as follows: the high temperature induced by the thermal shock treatment leads to the pyrolysis of the metal salts. CoS then recrystallizes into clusters on the defect sites of the graphene nanosheets. Next, the CoS clusters grow into ultrafine CoS nanoparticles, which catalyze the active carbon transformation into graphene on the CoS surface during the growth process, as shown in Fig. 1(b). The ultrashort shock time followed by the ultrafast cooling restricts the diffusion and migration of the as-formed CoS nanoparticles and enables uniform nanoparticle distribution across the graphene nanosheets. This CoS@ few-layer graphene core-shell structure can prevent the catalysts from being directly exposed to electrolyte, thereby preventing corrosion and improving the electrocatalytic performance. Moreover, strong and stable interfacial contacts between the core-shell nanoparticles and the RGO treated at $\sim 2,000$ K provide robust electrically conductive pathways to further enhance the catalytic performance. The RGO nanosheets are also found to be heteroatom-doped by N and S from thiourea in the *in-situ* synthesis process, leading to additional active sites [48, 49]. The formation and stabilization of the nanoparticles in the matrix occurs within ~ 7 ms, which is advantageous over traditional manufacturing methods [50–52]. We envision that the proposed core-shell compound nanomaterial synthesis method through ultrafast high temperature treatment can achieve roll-to-roll manufacturing (Fig. S2 in the ESM) and utilize solar energy heating for future commercial applications pertaining to clean energy. Benefiting from the highly conductive graphene coating and strong interaction between nanoparticles and graphene, the CoS@ few-layer

graphene core-shell nanocomposites exhibit excellent catalytic performance for overall water splitting. The present methodology can be universally applied to synthesize other transition metal chalcogenides with a few-layer graphene coating, as well as transition metals, transition metal alloys and other nanoscale composites.

2 Experimental

2.1 Materials synthesis

In a typical synthesis, 10 mg of cobalt acetate and 15 mg of thiourea were dissolved in 10 mL of deionized water and stirred at room temperature for 10 min. After that, 8 mg of graphene oxide ink synthesized by a modified Hummer's method was poured into the above solution under continuous stirring. The obtained solution was then sealed and sonicated for 20 min before it was casted on a clean glass slide. The GO film with precursors can be detached from the glass slide as a freestanding film after drying at 80 °C for 1 h in air. The freestanding film was then thermal pre-annealed in a tube furnace at 673 K under an argon atmosphere, which was used to trigger the thermal shocking induced by current pulse. After a high temperature thermal shock treatment at $\sim 2,000$ K, the as-synthesized film was cut into small pieces (6 mm \times 6 mm in size) for further electrochemical measurements. All chemicals were purchased from Sigma-Aldrich and used as received.

2.2 Materials characterization

The as-synthesized CoS-RGO electrocatalyst was characterized by a Hitachi SU-70 field emission scanning electron microscope (SEM) with an accelerating voltage of 15 kV. Transmission electron microscopy (TEM) was acquired by a JEOL JEM 2100F at an accelerating voltage of 200 kV. XPS measurements were performed on a Kratos Axis 165 X-ray photoelectron spectrometer. XRD pattern was obtained using the D8 Advanced (Bruker AXS, WI, USA).

2.3 Temperature measurements

The high temperature treatment was conducted by applying current pulse to the mounted CoS-RGO film in a vacuum chamber. Since

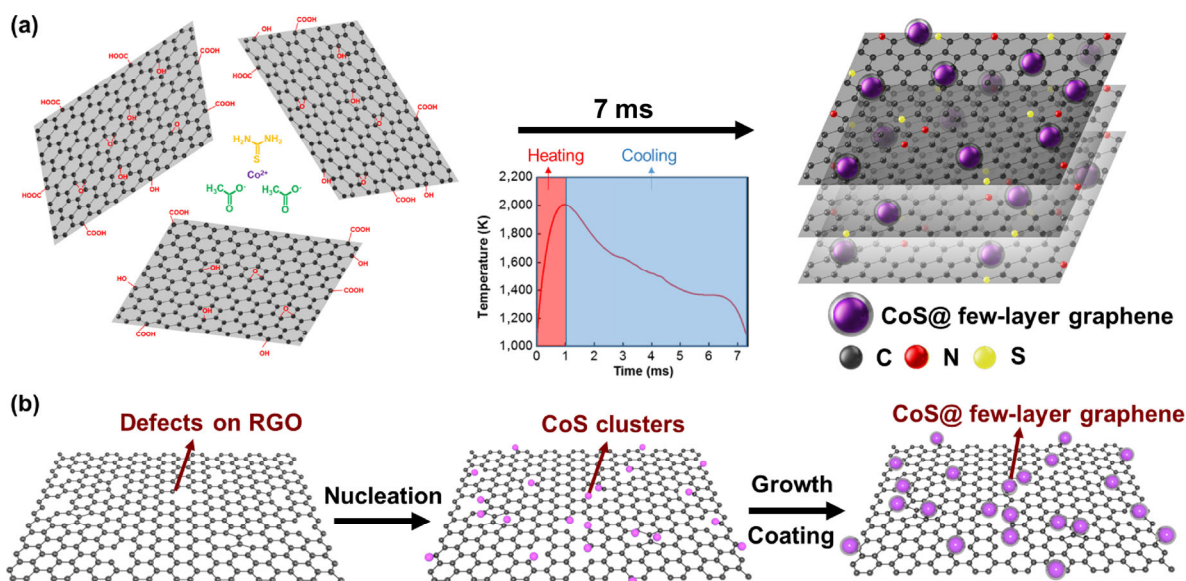


Figure 1 Schematic illustration of the synthesis of CoS@ few-layer graphene core-shell nanoparticle electrocatalysts within milliseconds. (a) Cobalt acetate, thiourea, and graphene oxide are transformed into ultrafine uniformly loaded CoS@ few-layer graphene core-shell nanoparticles on nitrogen- and sulfur-doped graphene after thermal shocking at $\sim 2,000$ K. The curve shows the temperature profile during the high temperature treatment. Note that the synthesis process can be finished within ~ 7 ms, and the heating and cooling times are ~ 1 and ~ 6 ms, respectively. (b) The formation mechanism of CoS@ few-layer graphene is proposed to involve the initial nucleation of CoS clusters on the defect sites of the graphene nanosheets that then grow into the ultrafine CoS nanoparticles, which catalyze the active carbon transformation into graphene on the CoS surface during the process. The ultrashort shock time followed by ultrafast cooling restricts the diffusion and migration of the as-formed CoS nanoparticles and enables uniform nanoparticle distribution across the graphene nanosheets.

the process was ultrafast, the diagnostics should have the capability to resolve the sub millisecond time scale. Therefore, the light emitting from the sample was collected and sent into a 0.5 m spectroscopy (Acton SP 500i) with a $150 \text{ l}\cdot\text{mm}^{-1}$ grating to disperse the light. The spectrum was collected by a 32 channel PMT array connected with a high-speed data acquisition system (Vertilon IQSP 580). The data acquisition was run over a wavelength of 508–853 nm, consisting of 27 channels of the PMT, and the system sensitivity was calibrated using up a black body furnace in the range of 1,200–1,500 K. In this construction, each channel collected light over a band of $\sim 13 \text{ nm}$ in wavelength. The sample rate on the system was set at 10 kHz, producing a sample every 100 microseconds, for the purpose of resolving the sub millisecond current pulse. The time resolved spectrums were subsequently fit to the black body radiation to obtain the temperature profile.

2.4 Electrochemical measurements

The electrochemical tests for HER and OER were performed in a conventional three electrode setup, with the CoS nanoparticle-embedded RGO sheets as the working electrode, a graphite rod as the counter electrode (HER), and a commercial Ag/AgCl electrode as the reference electrode. The CoS nanoparticle-embedded RGO film was directly used as the working electrode. The as-synthesized film was cut into small pieces with the size of $5 \text{ mm} \times 5 \text{ mm}$ and attached to an electrical wire using silver paste. Epoxy was employed as sealer to ensure no exposed silver paste or metal wire, which may contribute to the catalytic activity. The sample was then connected to the potentiostat for electrochemical test. The tests for HER and OER were performed in 1 M KOH as electrolyte. A linear sweep voltammetry with a scan rate of $2 \text{ mV}\cdot\text{s}^{-1}$ was applied for polarization to evaluate the activity of the material, while a high rate of $50 \text{ mV}\cdot\text{s}^{-1}$ was used for the stability test. In order to evaluate the bifunctionality of the system, a two electrode system was constructed, with CoS nanoparticle-embedded RGO as both the anode and the cathode. The scan rate for the linear sweep voltammetry was $2 \text{ mV}\cdot\text{s}^{-1}$ as well. The electrochemical tests were performed with a Bio-Logic EC-Lab electrochemistry tester.

2.5 Modeling

We performed first-principle DFT calculations by utilizing the SIESTA code [53]. The generalized gradient approximation in the framework of Perdew-Burke-Ernzerhof is adopted for the exchange-correlation potential. Numerical atomic orbitals with double zeta plus polarization are used for the basis set, with a plane-wave energy cutoff of 500 Ry. See ESM about slab models on different catalyst surfaces and associated Monkhorst-Pack K-points (For the model in main text, $1 \times 7 \times 5$ K-points are used). Self-consistent field tolerance is 10^{-4} . Geometry optimizations are first performed on structures before the run of molecular dynamics and calculation of density of states. Denser K-points were used for the electronic structure calculations (For the model in main text, $10 \times 70 \times 50$ K-points are used). The electronic smearing temperature during all calculations is 300 K.

In each round of AIMD simulation, one pair of a proton and an electron (an additional hydrogen atom) is added close to the catalyst surface in the system. Two pairs of protons and electrons (two additional hydrogen atoms) may be added for the starting round of simulation to minimize the number of simulation runs needed if the HER is to occur. The system is equilibrated at a temperature of 300 K using NVT Canonical ensemble for 4 ps, with a time step of 1 fs. When one round of simulation finishes, the final configuration of the system is extracted and modified by adding one proton and one electron close to the catalyst surface, then this modified configuration is the starting configuration for the next round of simulation.

3 Results and discussion

Figures 2(a) and 2(b) shows cobalt acetate and thiourea forming $\sim 1 \mu\text{m}$ clusters on the graphene oxide film. The large-scale graphene oxide film containing the cobalt acetate and thiourea mixture is prepared by a simple casting method, as illustrated in the inset image of Fig. 2(c). The ultrafast nature of the high temperature treatment was characterized by an in-house assembled spectropyrrometer. The light emitted by the heated sample was spectrally resolved by a $150 \text{ l}\cdot\text{mm}^{-1}$ grating and collected on a 32 channel photomultiplier tube (PMT) detector. A PMT detector was chosen over a charge coupled device (CCD) detector due to its higher dynamic range, higher sample rate and sensitivity, which allows signal capture with a much smaller acquisition time increment. The time resolved intensities on the first 27 channels (corresponding wavelengths: 853–508 nm) were acquired at a rate of 10 kHz to provide spectral information of the ultrafast heating process (Fig. 2(c)). The intensity peaks occur within the 7 ms time frame. The spectra were subsequently fit to Planck's law assuming a Greybody to obtain the corresponding temperature profile. The time resolved temperature, as shown in Fig. 1(b), was observed to closely follow the intensity profile on the 853 nm channel and did not show significant temperature reduction until $\sim 1 \text{ ms}$ into the synthesis (Fig. S3 in the ESM). Once the power supply was cut off, the sample cooled down in $\sim 7 \text{ ms}$ via conduction to the holder and radiation to the surroundings. Since the sensitivity of PMT is limited to the visible range, the lowest detectable temperature is about 1,000 K and as the intensity levels dropped with the sample cooling down, the signal to noise ratio was substantially reduced resulting in inaccurate temperature prediction.

The morphology of the as-prepared cobalt-sulfide nanoparticles is shown in Fig. 2(d) which reveals that the cobalt-sulfide nanoparticles are $\sim 20 \text{ nm}$ in diameter and uniformly distributed on the RGO nanosheets. A close view image in Fig. 2(e) shows that most of the nanoparticles are either spherical or ellipsoidal. Energy-dispersive X-ray spectroscopy (EDX) of a single nanoparticle presents the elements of C, Co, S with a Co/S atomic ratio of ~ 0.96 (Fig. S4 in the ESM), suggesting the main composition of the nanoparticle is CoS. The four strong peaks at 30.73° , 35.38° , 47.05° , 54.81° in the X-ray diffraction (XRD) pattern (Fig. 2(f)) can be assigned to the (100), (101), (102) and (110) crystal planes of CoS with a hexagonal structure, confirming the high crystallinity of CoS nanoparticles. The characteristic peak corresponding to (002) in graphite shows up around $\sim 26.05^\circ$, revealing the RGO layer-layer distance with a value of 0.342 nm. The elemental composition and electronic structure of the cobalt-sulfide nanoparticles on RGO nanosheets are investigated by X-ray photoelectron spectroscopy (XPS). All spectrums were calibrated to the 284.0 eV binding energy of sp^2 carbon. The XPS spectrum presents signals of C 1s, O 1s, Co 2p, S 2p and N 1s for CoS-RGO with atomic ratios of 79%, 12%, 1.5%, 3.5%, 3.9%, respectively (Fig. S5 in the ESM). The high-resolution Co 2p spectrum reveals two prominent bands at 796.4 and 780.8 eV (Fig. 2(g)), corresponding to Co 2p_{1/2} and Co 2p_{3/2}, respectively, which is consistent with the literature values of electron-binding energies of Co^{2+} cations in CoS [54]. In addition, the minor peaks that appeared at 777.9 and 792.9 eV should be assigned to Co-N bands, which indicates a Co-N compound formed in the high temperature treatment process. The high-resolution S 2p spectrum can be deconvoluted into four bands, which are centered at 161.2, 162.4, 163.3, and 164.5 eV (Fig. 2(h)). Among the binding energies, S 2p_{3/2} (161.2 eV) and S 2p_{1/2} (162.4 eV) correspond to the S^{2-} anions in CoS. The characteristic peaks of S 2p_{3/2} (163.3 eV) and S 2p_{1/2} (164.5 eV) can be assigned to S–C bonds, derived from sulfur doping on the RGO nanosheets. The ratio of S–Co bonds to S–C bonds is calculated from the corresponding areas to be around 53.8%, which suggests a sulfur dopant concentration of 1.58 at.% in the RGO matrix. The high-

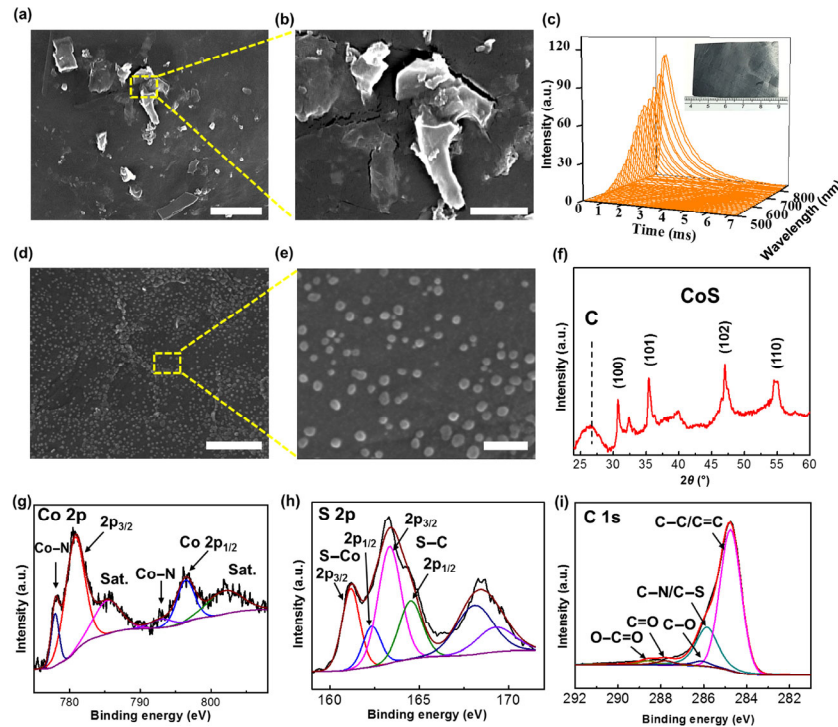


Figure 2 Characterization of the CoS nanoparticles. (a) SEM image showing cobalt acetate and thiourea particles on the graphene oxide nanosheets. Scale bar, 2 μm . (b) Detail of the surface morphology at higher magnification. Scale bar, 1 μm . (c) Emission spectra of the CoS-RGO film during the ultrafast heating process. Inset: large-scale graphene oxide film containing cobalt acetate and thiourea. (d) FESEM images of the as-prepared CoS nanoparticles, clearly revealing the uniform distribution of the CoS nanoparticles on the RGO nanosheets. Scale bar, 500 nm. (e) Detail of the surface morphology at higher magnification. Scale bar, 100 nm. (f) XRD patterns of the CoS nanoparticles. High-resolution (g) Co 2p, (h) S 2p, and (i) C 1s XPS spectrum of the CoS-RGO.

resolution N 1s spectrum can be resolved into four components which are assigned to pyridinic N (397.8 eV), pyrrolic N (399.3 eV), graphitic N (400.8 eV) and oxidized N (403.0 eV), with percentages of 56.7%, 22.3%, 14.0% and 6.9%, respectively (Fig. S6 in the ESM). From this measurement, pyridinic N is identified as the dominant N-doping component, which leads to great enhancement of catalytic performance of CoS for water splitting [55]. Sulfur and nitrogen dopants in the RGO nanosheets likely originate from excessive thiourea during the synthesis. After the N- and S-doping, the high-resolution C 1s spectrum can be fitted into five components with different binding energies, including: C–C/C=C (284.8 eV), C–N/C–S (285.9 eV), C–O (286.1 eV), C=O (287.8 eV), and O–C=O (288.6 eV), as shown in Fig. 2(i) [56].

The synthesized nanoparticles were further characterized by transmission electron microscopy (TEM), as shown in Fig. 3. A typical TEM image shows the uniform distribution of CoS nanoparticles on RGO nanosheets (Fig. 3(a)). An enlarged TEM image reveals that CoS nanoparticles with an average size of 20 nm were embedded in the two dimensional (2D) RGO nanosheets with strong adsorption (Fig. 3(b)). Remarkably, the CoS nanoparticles are coated with few-layer graphene with a thickness of ~ 2 nm as shown in the HRTEM image (Fig. 3(c)). This corresponds to 4–6 layers of graphene which may be formed by the recrystallization of active carbon atoms within the RGO film catalyzed by CoS during the ultrafast high temperature treatment. A graphene shell with an appropriate thickness can prevent the catalyst from being directly exposed to the electrolyte and corroding during long term operation, thereby improving the electrochemical stability performance. What is more, the few-layer graphene shell strongly promotes electron penetration from the core catalyst to the graphene surface, leading to superior catalytic activity on the graphene shell [57]. Atomic resolution TEM of a cobalt-sulfide nanoparticle clearly shows crystalline planes with an interplanar distance of 0.19 nm, which can be ascribed to (102) planes of CoS, confirming the excellent

crystallinity of the synthesized CoS nanoparticles (Fig. 3(d)). EDX elemental mappings of a CoS nanoparticle illustrate the homogeneous distribution of Co and S atoms across the RGO nanosheets, demonstrating the uniform atomic mixture of Co and S atoms in as-synthesized particles (Figs. 3(e)–3(g)). In subsequent tests, we demonstrated that the size and distribution of nanoparticles can be controlled by varying experimental parameters, such as the thermal shock duration. For instance, CoS nanoparticles centered between 50–100 nm can be synthesized after a 5 min thermal shock (Fig. S7 in the ESM), while ~ 20 nm CoS nanoparticles are produced by a 7 ms thermal shock. The heating and cooling rate and thermal shock temperature also play important roles in nanoparticle formation (Figs. S8 and S9 in the ESM). Compared with the ultrafast thermal shock with the heating and cooling rate on the order of 10^5 – 10^6 $\text{K}\cdot\text{s}^{-1}$, the slow heating (~ 10 $\text{K}\cdot\text{s}^{-1}$ heating and instant cooling) or cooling (instant heating and ~ 10 $\text{K}\cdot\text{s}^{-1}$ cooling) leads to CoS nanoparticles which suffer from serious aggregation and much thicker carbon coating (Fig. S8 in the ESM). The aggregation of nanoparticles should originate from the loss of defects through the long residence at high temperature and adequate time for particle migration. The thicker carbon coating should be caused by the sufficient growth time of active carbon.

The HER activity of the synthesized catalyst is evaluated in a typical three-electrode cell setup. The freestanding RGO-CoS film is directly employed as the working electrode. Figures 4(a) and 4(b) show the polarization curves and Tafel plots of the CoS-RGO electrocatalyst with a mass loading of 0.5 $\text{mg}\cdot\text{cm}^{-2}$ in 1 M KOH solution, along with 40 wt.% Pt/C catalyst for reference. The CoS-RGO exhibits excellent HER activity with the lowest onset overpotential of ~ 37 mV versus a reversible hydrogen electrode (RHE). Small overpotentials of 51, 118, and 226 mV are required for the CoS-RGO electrocatalyst to reach -1 , -10 , and -100 $\text{mA}\cdot\text{cm}^{-2}$ cathodic currents (Fig. 4(a)), respectively, which outperforms the 40 wt.% Pt/C catalyst with rapidly rising cathodic current, making it among the most

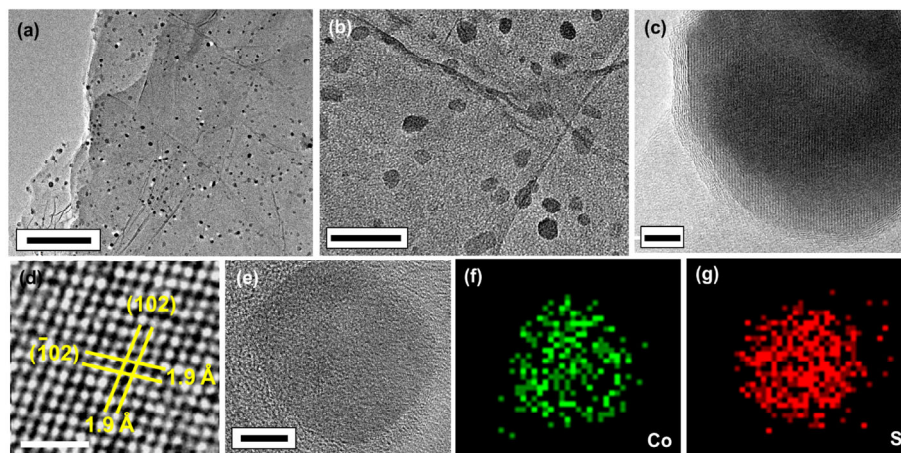


Figure 3 Characterizations of CoS@ few-layer graphene core-shell nanoparticles. (a) TEM image of cobalt-sulfide nanoparticles. Scale bar, 500 nm. (b) Magnified TEM image. Scale bar, 100 nm. (c) HRTEM image of a single cobalt-sulfide nanoparticle, presenting crystal nanoparticle surrounded by graphene shells with a thickness of ~ 2 nm. Scale bar, 5 nm. (d) Atomic resolution TEM image of a CoS nanoparticle, revealing clear crystalline (102), ($\bar{1}02$) planes with a d -spacing of 0.19 nm. Scale bar, 1 nm. (e)–(g) TEM image of cobalt-sulfide nanoparticle and the corresponding EDX elemental mapping of elements Co and S. Scale bar in (e) is 5 nm.

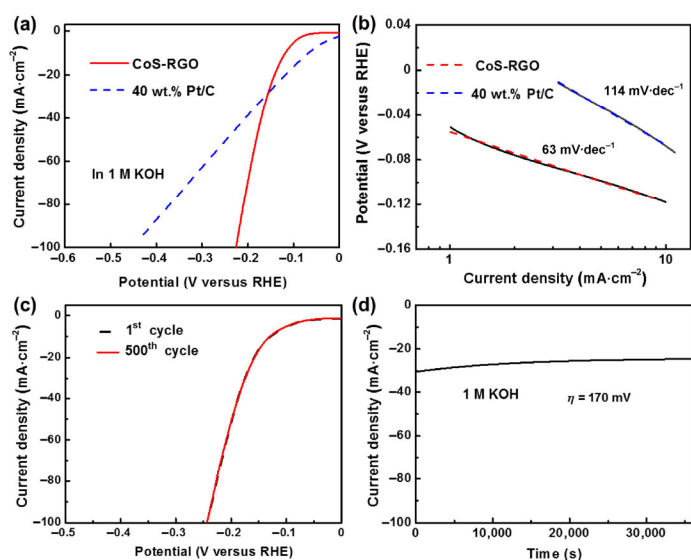


Figure 4 HER performance of CoS-RGO electrocatalyst in 1 M KOH. (a) The HER polarization curves of CoS-RGO compared with 40% Pt/C at $2 \text{ mV}\cdot\text{s}^{-1}$ in 1 M KOH. (b) Tafel plot of CoS-RGO. (c) Polarization curves after continuous potential sweeps at $50 \text{ mV}\cdot\text{s}^{-1}$ in 1 M KOH. (d) Time dependence of the cathodic current density during electrolysis under $\eta = 170 \text{ mV}$ in 1 M KOH.

active non-noble material based electrocatalysts at basic conditions. The corresponding Tafel plot, as depicted in Fig. 4(b), shows a small Tafel slope of $\sim 63 \text{ mV}\cdot\text{dec}^{-1}$ for CoS-RGO, which is higher than $51 \text{ mV}\cdot\text{dec}^{-1}$ for the 40 wt.% Pt/C electrocatalyst, suggesting a Volmer-Heyrovsky reaction mechanism.

Stability is always a critical aspect in catalyst evaluation for long-term application. To assess the durability of the CoS-RGO electrocatalyst in basic conditions, accelerated linear potential sweeps were carried out continuously at a scan rate of $50 \text{ mV}\cdot\text{s}^{-1}$ (Fig. 4(c)). The polarization curve shows a negligible decay after 500 repeated potential sweeps, which implies that the catalyst is highly stable without any obvious corrosion. Furthermore, the stability of the electrocatalyst is evaluated by electrolysis at fixed potentials over prolonged periods. A stable current density of $\sim 30 \text{ mA}\cdot\text{cm}^{-2}$ was observed after 10 h testing at an overpotential of 170 mV (Fig. 4(d)), confirming the outstanding electrochemical stability of CoS-RGO in basic condition. The HER activity of CoS-RGO in acidic condition is shown in Figs. S10–S12 in the ESM.

The OER activity of the CoS-RGO electrocatalyst is also investigated in 1 M KOH, as shown in Figs. 5(a) and 5(b). The linear sweep

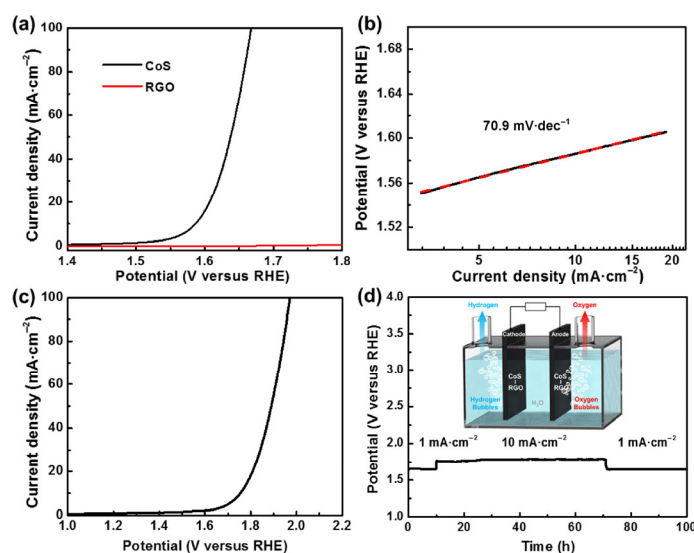


Figure 5 Bifunctional CoS@ few-layer graphene core-shell nanoparticles for two-electrode water splitting. (a) The OER polarization curves of CoS-RGO with a loading mass of $0.5 \text{ mg}\cdot\text{cm}^{-2}$ and RGO in 1 M KOH. The CoS-RGO exhibits significantly improved OER performance than RGO. (b) Tafel plot of CoS-RGO. (c) CoS-RGO as HER and OER bifunctional catalysts in 1 M KOH for overall water splitting. (d) Long-term stability of the CoS-RGO bifunctional catalyst with a loading mass of $0.5 \text{ mg}\cdot\text{cm}^{-2}$. Inset: schematic showing the two-electrode cell setup for the overall water splitting reaction.

of CoS-RGO (Fig. 5(a)) shows that small potentials of ~ 1.58 and 1.66 V versus RHE are required to drive 10 and $100 \text{ mA}\cdot\text{cm}^{-2}$ cathodic current, respectively, which is comparable to Ir-C ($20 \text{ wt.}\% \text{ Ir}$) [58], indicating the superior electrocatalytic property for OER (comparison with state-of-the-art non-noble metal based catalysts can be found in Table S2 in the ESM). In contrast, pure RGO exhibits negligible current in the measured potential range, suggesting the negligible contribution of pure RGO for OER. The small Tafel slope of $\sim 71 \text{ mV}\cdot\text{dec}^{-1}$ confirms the excellent catalyst performance of CoS-RGO for OER, which compares favorably to the reported Pt/C catalyst ($118 \text{ mV}\cdot\text{dec}^{-1}$) [59]. To investigate the feasibility of employing CoS-RGO as an efficient bifunctional catalysts for both OER and HER simultaneously, a CoS-RGO free-standing electrode was fabricated as both the anode and cathode in a two-electrode cell setup in 1 M KOH solution (Fig. 5(c)). The electrolysis using CoS-RGO as a bifunctional catalyst demonstrates impressive performance for overall water splitting. Small potentials of ~ 1.75 and 1.97 V are required for

CoS-RGO to reach 10 and 100 mA·cm⁻² anodic current, respectively, which is superior to that reported for Pt electrocatalysts [60] (comparison with state-of-the-art non-noble metal based catalysts can be found in Table S3 and Fig. S13 in the ESM). The long-term stability is tested by electrolysis at fixed current density, (1 and 10 mA·cm⁻²) for 100 h (Fig. 5(d)). The voltage stabilizes at ~ 1.64 V to achieve 1 mA·cm⁻² current for 10 h continuous operation, then stabilizes at ~ 1.78 V to achieve 10 mA·cm⁻² current for 60 h continuous operation. After switching the current density back to 1 mA·cm⁻², the voltage again stabilizes at ~ 1.64 V, indicating no structure change of the active catalysts even after 60 h of operation under high current density. The remarkable stability at different current densities without any decay illustrates the advantage of few-layer graphene coated CoS nanoparticles on RGO for overall water splitting. In comparison, the synthesized CoS nanoparticles on a carbon fiber network (CF) without graphene showed visible decay of HER activity after only three cycles (Fig. S14 in the ESM), depicting the poor stability of CoS-CF without graphene protection. The excellent electrocatalytic performance of CoS-RGO should be attributed to the chemical composition and structure of the synthesized CoS@ few-layer graphene core-shell nanoparticles grown on N and S doped RGO nanosheets. Note that the N- and S-doping introduces defects on RGO nanosheets to form additional catalytic sites, which are beneficial to the catalytic performance for water splitting. Additionally, the small amount of N-doping in CoS (Co–N bond) may have a minor contribution to the electrocatalytic performance.

We then aimed to provide a first-step computational understanding of the catalytic properties of CoS for overall water splitting by investigating the HER process in an acidic environment, which is the simplest case. Available literatures [57, 61] have shown that the enhanced HER performance in the presence of a graphene shell originates from the modulation of the electron density and the electronic potential distribution at the graphene surface by a penetrating electron from the catalyst core. The graphene region in contact with the catalyst's active sites is more active than the region without contact. We think that a similar electron modulation mechanism could be effective in our system. As a first-step, the computational studies in this current work focus more on the active sites of the CoS surface, as we do not explicitly model the influence of the few-layer graphene shell. Future computational efforts are needed to explicitly address the enhancing effect of graphene on HER and OER in acidic and alkaline solution.

HER ($2\text{H}^+ + 2\text{e}^- = \text{H}_2$) is a multi-step electrochemical process taking places on the surface of a catalyst [62–65]. In acid solution, it is generally accepted that the Volmer reaction happens first. This reaction is the combination of a proton and an electron on the catalyst surface which results in an adsorbed hydrogen atom, and can be expressed as $\text{H}^+ + \text{C} + \text{e}^- = \text{CH}_{\text{ads}}$, where C denotes the catalyst surface. The next step has two scenarios. The first is the Heyrovsky reaction. The adsorbed hydrogen atom combines with a proton and an electron to produce hydrogen molecule, and can be expressed as $\text{CH}_{\text{ads}} + \text{H}^+ + \text{e}^- = \text{C} + \text{H}_2$. The second is the Tafel reaction. Two adsorbed hydrogen atoms evolve to produce hydrogen molecule, and can be expressed as $\text{CH}_{\text{ads}} + \text{CH}_{\text{ads}} = 2\text{C} + \text{H}_2$. To shed light on the HER mechanism, we carried out a series of *ab initio* molecular dynamic (AIMD) studies to explore the details of the catalytic steps at the water catalyst interface (model details and additional data are available in the Experimental section and ESM). We have examined several surfaces with distinct distributions of S or Co atoms to evaluate the preference of active sites on the catalyst surface (i.e., Fig. S15 in the ESM). Figure 6 summarizes the results for a surface that has both S and Co atoms exposed. The Volmer reactions are observed during each round of AIMD simulations (Fig. S16 in the ESM). Figures 6(a)–6(c) show a repre-

sentative Volmer reaction right before the production of H₂. Figure 6(a) shows the initial configuration of the system in which there are pre-adsorbed hydrogen atoms on Co and S (marked by brown and green circles) from previous rounds of adsorption. A hydronium ion (H₃O⁺) is present near the catalyst surface. Figure 6(b) shows that a pre-adsorbed H on Co (marked by brown circle) is first attracted towards the hydronium ion and then moves a little bit away from the catalyst surface. An extra H (proton, marked by grey circle) in the hydronium ion is also attracted towards the catalyst surface and detaches from the water molecule. They evolve closer to each other, but eventually both are adsorbed on to the catalyst surface, as Fig. 6(c) shows. The pre-adsorbed H (marked by brown circle) atom returns to its initial adsorption site between two Co atoms, while the proton is adsorbed to the top of a Co atom after combining with an electron. Such a reaction is essentially the Volmer reaction. The involvement of the other pre-adsorbed H atom approaching the proton makes such a reaction almost Heyrovsky-type, which produces a hydrogen molecule. Nevertheless, the failure to produce molecular hydrogen seems to suggest that Co may not be an active site for HER. Figures 6(d)–6(f) to 6f show a representative Heyrovsky reaction. Figure 6(d) shows that the adsorbed H on S (marked by green circle) in Fig. 6(c) is attracted towards the hydronium ion and detaches from the catalyst surface. In the meantime, the proton (marked by purple circle) in the hydronium ion approaches the detached H from the catalyst surface (Fig. 6(e)). Combining with an electron, eventually, a hydrogen molecule is produced and stably exists in the system (Fig. 6(f)). Compared with the trajectory described in Figs. 6(a)–6(c), such a successful production of a hydrogen molecule seems to suggest that S, instead of Co, is an active site for HER. This conclusion is further verified by density

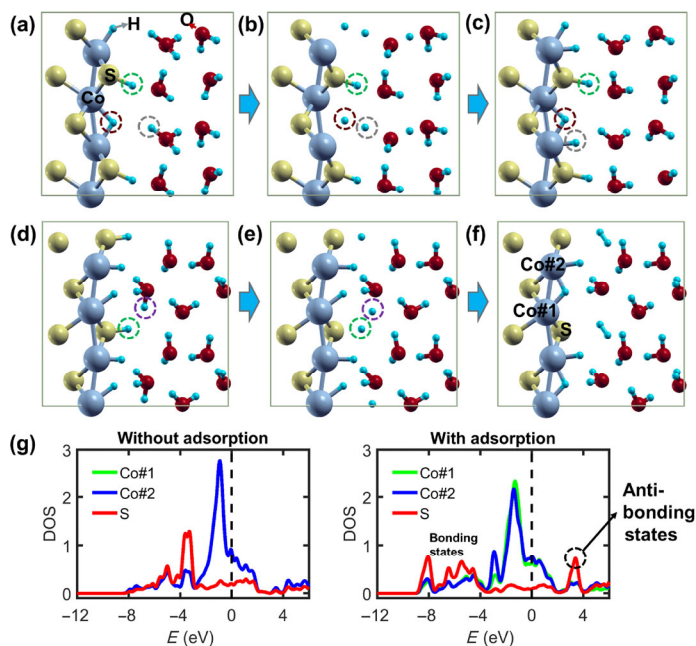


Figure 6 DFT calculations for HER on CoS. (a)–(c): *Ab initio* molecular dynamics simulation (AIMD) revealing a Volmer reaction. The H marked by the green and brown circles are adsorbed onto the surface during previous rounds of adsorption. The H marked by the grey circle, provided by a hydronium ion in the current round of adsorption, is further adsorbed onto the Co site. (d)–(f): AIMD revealing a Heyrovsky reaction. The combination of the H marked by the purple circle from the hydronium ion and the adsorbed H on S marked by the green circle produces a hydrogen molecule. (g) Projected Density of States (DOS) of three atoms on the surface, as labeled in (f). The green line in the DOS without adsorption is completely overlaps with the blue due to the structural symmetry. The dashed line denotes the Fermi level. The strong anti-bonding states of S upon hydrogen adsorption emerging above the Fermi level suggest that S is the active reaction site.

of states (DOS) analyses and additional calculations on other types of surfaces. The catalytic property of a catalyst is determined fundamentally by its electronic structure [65–67], thus we have calculated the electronic DOS at several sites on the investigated surfaces (Fig. S16 in the ESM), as labeled by Co#1, Co#2, and S in Fig. 6(f), and the results are compared with the case without adsorption. As shown in Fig. 6(g), upon hydrogen adsorption, there is a strong peak of anti-bonding states of S emerging above the Fermi level. Such a feature is in line with the DOS calculation for Pt, which is usually used as a HER catalyst [68]. On the contrary, there is no apparent peak of anti-bonding states of Co emerging above the Fermi level upon hydrogen adsorption. It is thus reasonable to conclude that S is the major active reaction sites for the surface as shown in Fig. 6. Further calculations on other surfaces (Figs. S18 and S19 in the ESM) have also demonstrated that S is the dominant active reaction site.

4 Conclusion

In summary, we have developed a low-cost and scalable approach to synthesize evenly distributed and ultrafine CoS nanoparticle electrocatalysts on RGO nanosheets in an extremely short time (~ 7 ms), simply by applying current through the precursors to achieve a high temperature (~ 2,000 K). The resultant CoS@ few-layer graphene core-shell nanoparticles exhibit remarkable electrocatalytic activity and stability for both HER and OER as bifunctional electrodes in an overall water splitting configuration. Typically, the bifunctional catalysts deliver a current of 10 mA·cm⁻² at ~ 1.77 V as well as superior stability in a two-electrode cell setup and 1 M KOH solution, which is comparable with the best bifunctional electrocatalyst previously reported. The exceptional electrocatalytic activity is largely attributed to the chemical composition and structure of the synthesized CoS@ few-layer graphene core-shell nanoparticles, as well as the interaction effect of the N- and S-doping atoms on the RGO substrate. This work illustrates a facile strategy to rapidly fabricate efficient CoS@ few-layer graphene core-shell nanoparticle electrocatalysts, which can be generally applicable for synthesizing other functional nanomaterials, thus opening a new route for developing high-performance electrocatalysts for practical energy conversion applications.

Acknowledgement

This project is supported by the NSF Scalable Nanomanufacturing Project #1635221 (entitled “SNM: Continuous Synthesis and Stabilization of Nanoparticles in a Carbon Matrix Using Rapid Thermal Shock”). We acknowledge the support of the Maryland NanoCenter and its AIMLab. Y. N. C. would like to acknowledge the China Scholarship Council (CSC) for financial support. Partial support for M. R. Z. and R. J. J. comes from an ONR-MURI grant.

Electronic Supplementary Material: Supplementary material (additional material characterization such as EDX, SEM images and electrochemical results such as HER polarization curves, the Tafel plot and the turnover frequency, tables on comparisons of electrochemical performances, simulation details) is available in the online version of this article at <https://doi.org/10.1007/s12274-019-2304-0>.

Author contributions

Y. C. and L. H. conceived the idea of ultrafast cobalt chalcogenide nanoparticle formation and designed the experiment. Y. C. and S. X. conducted the catalytic characterization. R. J. and M. Z. collected the ultrafast temperature profiles. S. Z. and T. L. carried out the computational modeling. All authors contributed to writing the manuscript.

References

- [1] Larcher, D.; Tarascon, J. M. Towards greener and more sustainable batteries for electrical energy storage. *Nat. Chem.* **2015**, *7*, 19–29.
- [2] Liu, C.; Tang, J. Y.; Chen, H. M.; Liu, B.; Yang, P. D. A fully integrated nanosystem of semiconductor nanowires for direct solar water splitting. *Nano Lett.* **2013**, *13*, 2989–2992.
- [3] Dresselhaus, M. S.; Thomas, I. L. Alternative energy technologies. *Nature* **2001**, *414*, 332–337.
- [4] Li, W.; He, D.; Sheehan, S. W.; He, Y. M.; Thorne, J. E.; Yao, X. H.; Brudvig, G. W.; Wang, D. W. Comparison of heterogenized molecular and heterogeneous oxide catalysts for photoelectrochemical water oxidation. *Energy Environ. Sci.* **2016**, *9*, 1794–1802.
- [5] Yang, X. G.; Liu, R.; He, Y. M.; Thorne, J.; Zheng, Z.; Wang, D. W. Enabling practical electrocatalyst-assisted photoelectron-chemical water splitting with earth abundant materials. *Nano Res.* **2015**, *8*, 56–81.
- [6] Zheng, N. F.; Bu, X. H.; Vu, H.; Feng, P. Y. Open-framework chalcogenides as visible-light photocatalysts for hydrogen generation from water. *Angew. Chem.* **2005**, *117*, 5433–5437.
- [7] Zeng, M.; Li, Y. G. Recent advances in heterogeneous electrocatalysts for the hydrogen evolution reaction. *J. Mater. Chem. A* **2015**, *3*, 14942–14962.
- [8] Li, X. M.; Hao, X. G.; Abudula, A.; Guan, G. Q. Nanostructured catalysts for electrochemical water splitting: Current state and prospects. *J. Mater. Chem. A* **2016**, *4*, 11973–12000.
- [9] Walter, M. G.; Warren, E. L.; McKone, J. R.; Boettcher, S. W.; Mi, Q. X.; Santori, E. A.; Lewis, N. S. Solar water splitting cells. *Chem. Rev.* **2010**, *110*, 6446–6473.
- [10] Lee, Y.; Suntivich, J.; May, K. J.; Perry, E. E.; Shao-Horn, Y. Synthesis and activities of rutile IrO₂ and RuO₂ nanoparticles for oxygen evolution in acid and alkaline solutions. *J. Phys. Chem. Lett.* **2012**, *3*, 399–404.
- [11] Zou, X. X.; Zhang, Y. Noble metal-free hydrogen evolution catalysts for water splitting. *Chem. Soc. Rev.* **2015**, *44*, 5148–5180.
- [12] Faber, M. S.; Jin, S. Earth-abundant inorganic electrocatalysts and their nanostructures for energy conversion applications. *Energy Environ. Sci.* **2014**, *7*, 3519–3542.
- [13] Wang, P. T.; Zhang, X.; Zhang, J.; Wan, S.; Guo, S. J.; Lu, G.; Yao, J. L.; Huang, X. Q. Precise tuning in platinum-nickel/nickel sulfide interface nanowires for synergistic hydrogen evolution catalysis. *Nat. Commun.* **2017**, *8*, 14580.
- [14] Li, H. Y.; Chen, S. M.; Jia, X. F.; Xu, B.; Lin, H. F.; Yang, H. Z.; Song, L.; Wang, X. Amorphous nickel-cobalt complexes hybridized with 1t-phase molybdenum disulfide via hydrazine-induced phase transformation for water splitting. *Nat. Commun.* **2017**, *8*, 15377.
- [15] Xu, S. M.; Chen, Y. N.; Li, Y. J.; Lu, A. J.; Yao, Y. G.; Dai, J. Q.; Wang, Y. B.; Liu, B. Y.; Lacey, S. D.; Pastel, G. R. et al. Universal, *in situ* transformation of bulky compounds into nanoscale catalysts by high-temperature pulse. *Nano Lett.* **2017**, *17*, 5817–5822.
- [16] Zhou, Y. C.; Leng, Y. H.; Zhou, W. J.; Huang, J. L.; Zhao, M. W.; Zhan, J.; Feng, C. H.; Tang, Z. H.; Chen, S. W.; Liu, H. Sulfur and nitrogen self-doped carbon nanosheets derived from peanut root nodules as high-efficiency non-metal electrocatalyst for hydrogen evolution reaction. *Nano Energy* **2015**, *16*, 357–366.
- [17] Brown, D. E.; Mahmood, M. N.; Man, M. C. M.; Turner, A. K. Preparation and characterization of low overvoltage transition metal alloy electrocatalysts for hydrogen evolution in alkaline solutions. *Electrochim. Acta* **1984**, *29*, 1551–1556.
- [18] Wu, H. B.; Xia, B. Y.; Yu, L.; Yu, X. Y.; Lou, X. W. Porous molybdenum carbide nano-octahedrons synthesized via confined carburization in metal-organic frameworks for efficient hydrogen production. *Nat. Commun.* **2015**, *6*, 6512.
- [19] Xu, X. B.; Nosheen, F.; Wang, X. Ni-decorated molybdenum carbide hollow structure derived from carbon-coated metal-organic framework for electrocatalytic hydrogen evolution reaction. *Chem. Mater.* **2016**, *28*, 6313–6320.
- [20] Lu, Q. P.; Yu, Y. F.; Ma, Q. L.; Chen, B.; Zhang, H. 2D transition-metal-dichalcogenide-nanosheet-based composites for photocatalytic and electrocatalytic hydrogen evolution reactions. *Adv. Mater.* **2016**, *28*, 1917–1933.
- [21] Chen, J. Z.; Wu, X. J.; Yin, L. S.; Li, B.; Hong, X.; Fan, Z. X.; Chen, B.; Xue, C.; Zhang, H. One-pot synthesis of CdS nanocrystals hybridized

- with single-layer transition-metal dichalcogenide nanosheets for efficient photocatalytic hydrogen evolution. *Angew. Chem., Int. Ed.* **2015**, *54*, 1210–1214.
- [22] Lukowski, M. A.; Daniel, A. S.; Meng, F.; Forticaux, A.; Li, L. S.; Jin, S. Enhanced hydrogen evolution catalysis from chemically exfoliated metallic MoS₂ nanosheets. *J. Am. Chem. Soc.* **2013**, *135*, 10274–10277.
- [23] Wang, H. T.; Lu, Z. Y.; Kong, D. S.; Sun, J.; Hymel, T. M.; Cui, Y. Electrochemical tuning of MoS₂ nanoparticles on three-dimensional substrate for efficient hydrogen evolution. *ACS Nano* **2014**, *8*, 4940–4947.
- [24] Xie, J. F.; Zhang, H.; Li, S.; Wang, R. X.; Sun, X.; Zhou, M.; Zhou, J. F.; Lou, X. W.; Xie, Y. Defect-rich MoS₂ ultrathin nanosheets with additional active edge sites for enhanced electrocatalytic hydrogen evolution. *Adv. Mater.* **2013**, *25*, 5807–5813.
- [25] Tan, Y. W.; Liu, P.; Chen, L. Y.; Cong, W. T.; Ito, Y.; Han, J. H.; Guo, X. W.; Tang, Z.; Fujita, T.; Hirata, A. et al. Monolayer MoS₂ films supported by 3D nanoporous metals for high-efficiency electrocatalytic hydrogen production. *Adv. Mater.* **2014**, *26*, 8023–8028.
- [26] Duan, J. J.; Chen, S.; Chambers, B. A.; Andersson, G. G.; Qiao, S. Z. 3D WS₂ nanolayers@heteroatom-doped graphene films as hydrogen evolution catalyst electrodes. *Adv. Mater.* **2015**, *27*, 4234–4241.
- [27] Voiry, D.; Yang, J.; Chhowalla, M. Recent strategies for improving the catalytic activity of 2D TMD nanosheets toward the hydrogen evolution reaction. *Adv. Mater.* **2016**, *28*, 6197–6206.
- [28] Voiry, D.; Fullon, R.; Yang, J.; de Carvalho Castro e Silva, C.; Kappera, R.; Bozkurt, I.; Kaplan, D.; Lagos, M. J.; Batson, P. E.; Gupta, G. et al. The role of electronic coupling between substrate and 2D MoS₂ nanosheets in electrocatalytic production of hydrogen. *Nat. Mater.* **2016**, *15*, 1003–1009.
- [29] Miao, J. W.; Xiao, F. X.; Yang, H. B.; Khoo, S. Y.; Chen, J. Z.; Fan, Z. X.; Hsu, Y. Y.; Chen, H. M.; Zhang, H.; Liu, B. Hierarchical Ni-Mo-S nanosheets on carbon fiber cloth: A flexible electrode for efficient hydrogen generation in neutral electrolyte. *Sci. Adv.* **2015**, *1*, 1500259.
- [30] Ma, C. B.; Qi, X. Y.; Chen, B.; Bao, S. Y.; Yin, Z. Y.; Wu, X. J.; Luo, Z. M.; Wei, J.; Zhang, H. L.; Zhang, H. MoS₂ nanoflower-decorated reduced graphene oxide paper for high-performance hydrogen evolution reaction. *Nanoscale* **2014**, *6*, 5624–5629.
- [31] Chen, Y. N.; Xu, S. M.; Li, Y. C.; Jacob, R. J.; Kuang, Y. D.; Liu, B. Y.; Wang, Y. L.; Pastel, G.; Salamanca-Riba, L. G.; Zachariah, M. R. et al. FeS₂ nanoparticles embedded in reduced graphene oxide toward robust, high-performance electrocatalysts. *Adv. Energy Mater.* **2017**, *7*, 1700482.
- [32] Pi, Y. C.; Shao, Q.; Wang, P. T.; Lv, F.; Guo, S. J.; Guo, J.; Huang, X. Q. Trimetallic oxyhydroxide coraloids for efficient oxygen evolution electrocatalysis. *Angew. Chem.* **2017**, *129*, 4573–4577.
- [33] Yang, H. B.; Miao, J. W.; Hung, S. F.; Chen, J. Z.; Tao, H. B.; Wang, X. Z.; Zhang, L. P.; Chen, R.; Gao, J. J.; Chen, H. M. et al. Identification of catalytic sites for oxygen reduction and oxygen evolution in N-doped graphene materials: Development of highly efficient metal-free bifunctional electrocatalyst. *Sci. Adv.* **2016**, *2*, e1501122.
- [34] Zhang, J. T.; Zhao, Z. H.; Xia, Z. H.; Dai, L. M. A metal-free bifunctional electrocatalyst for oxygen reduction and oxygen evolution reactions. *Nat. Nanotechnol.* **2015**, *10*, 444–452.
- [35] Suntivich, J.; May, K. J.; Gasteiger, H. A.; Goodenough, J. B.; Shao-Horn, Y. A perovskite oxide optimized for oxygen evolution catalysis from molecular orbital principles. *Science* **2011**, *334*, 1383–1385.
- [36] Ma, T. Y.; Dai, S.; Jaroniec, M.; Qiao, S. Z. Metal-organic framework derived hybrid Co₃O₄-carbon porous nanowire arrays as reversible oxygen evolution electrodes. *J. Am. Chem. Soc.* **2014**, *136*, 13925–13931.
- [37] Gong, M.; Li, Y. G.; Wang, H. L.; Liang, Y. Y.; Wu, J. Z.; Zhou, J. G.; Wang, J.; Regier, T.; Wei, F.; Dai, H. J. An advanced Ni-Fe layered double hydroxide electrocatalyst for water oxidation. *J. Am. Chem. Soc.* **2013**, *135*, 8452–8455.
- [38] Cao, F. F.; Zhao, M. T.; Yu, Y. F.; Chen, B.; Huang, Y.; Yang, J.; Cao, X. H.; Lu, Q. P.; Zhang, X.; Zhang, Z. C. et al. Synthesis of two-dimensional CoS_{1.097}/nitrogen-doped carbon nanocomposites using metal-organic framework nanosheets as precursors for supercapacitor application. *J. Am. Chem. Soc.* **2016**, *138*, 6924–6927.
- [39] Xu, Y. Q.; Hao, Y. C.; Zhang, G. X.; Jin, X. Y.; Wang, L.; Lu, Z. Y.; Sun, X. M. One-step scalable production of Co_{1-x}S/graphene nanocomposite as high-performance bifunctional electrocatalyst. *Part. Part. Syst. Charact.* **2016**, *33*, 569–575.
- [40] Gao, M. R.; Xu, Y. F.; Jiang, J.; Yu, S. H. Nanostructured metal chalcogenides: Synthesis, modification, and applications in energy conversion and storage devices. *Chem. Soc. Rev.* **2013**, *42*, 2986–3017.
- [41] Faber, M. S.; Dziejdzic, R.; Lukowski, M. A.; Kaiser, N. S.; Ding, Q.; Jin, S. High-performance electrocatalysis using metallic cobalt pyrite (CoS₂) micro- and nanostructures. *J. Am. Chem. Soc.* **2014**, *136*, 10053–10061.
- [42] Kong, D. S.; Cha, J. J.; Wang, H. T.; Lee, H. R.; Cui, Y. First-row transition metal dichalcogenide catalysts for hydrogen evolution reaction. *Energy Environ. Sci.* **2013**, *6*, 3553–3558.
- [43] Kong, D. S.; Wang, H. T.; Lu, Z. Y.; Cui, Y. CoSe₂ Nanoparticles grown on carbon fiber paper: An efficient and stable electrocatalyst for hydrogen evolution reaction. *J. Am. Chem. Soc.* **2014**, *136*, 4897–4900.
- [44] Peng, S. J.; Li, L. L.; Han, X. P.; Sun, W. P.; Srinivasan, M.; Mhaisalkar, S. G.; Cheng, F. Y.; Yan, Q.; Chen, J.; Ramakrishna, S. Cobalt sulfide nanosheet/graphene/carbon nanotube nanocomposites as flexible electrodes for hydrogen evolution. *Angew. Chem., Int. Ed.* **2014**, *53*, 12594–12599.
- [45] Cabán-Acevedo, M.; Stone, M. L.; Schmidt, J. R.; Thomas, J. G.; Ding, Q.; Chang, H. C.; Tsai, M. L.; He, J. H.; Jin, S. Efficient hydrogen evolution catalysis using ternary pyrite-type cobalt phosphosulphide. *Nat. Mater.* **2015**, *14*, 1245–1251.
- [46] Luo, Z. M.; Tan, C. L.; Zhang, X.; Chen, J. Z.; Cao, X. H.; Li, B.; Zong, Y.; Huang, L.; Huang, X.; Wang, L. H. et al. Preparation of cobalt sulfide nanoparticle-decorated nitrogen and sulfur Co-doped reduced graphene oxide aerogel used as a highly efficient electrocatalyst for oxygen reduction reaction. *Small* **2016**, *12*, 5920–5926.
- [47] Sun, Y. J.; Liu, C.; Grauer, D. C.; Yano, J.; Long, J. R.; Yang, P. D.; Chang, C. J. Electrodeposited cobalt-sulfide catalyst for electrochemical and photoelectrochemical hydrogen generation from water. *J. Am. Chem. Soc.* **2013**, *135*, 17699–17702.
- [48] Ito, Y.; Cong, W. T.; Fujita, T.; Tang, Z.; Chen, M. W. High catalytic activity of nitrogen and sulfur Co-doped nanoporous graphene in the hydrogen evolution reaction. *Angew. Chem., Int. Ed.* **2015**, *54*, 2131–2136.
- [49] Wang, X. W.; Sun, G. Z.; Routh, P.; Kim, D. H.; Huang, W.; Chen, P. Heteroatom-doped graphene materials: Syntheses, properties and applications. *Chem. Soc. Rev.* **2014**, *43*, 7067–7098.
- [50] Chen, Y. N.; Egan, G. C.; Wan, J. Y.; Zhu, S. Z.; Jacob, R. J.; Zhou, W. B.; Dai, J. Q.; Wang, Y. B.; Danner, V. A.; Yao, Y. G. et al. Ultra-fast self-assembly and stabilization of reactive nanoparticles in reduced graphene oxide films. *Nat. Commun.* **2016**, *7*, 12332.
- [51] Chen, Y. N.; Li, Y. J.; Wang, Y. B.; Fu, K.; Danner, V. A.; Dai, J. Q.; Lacey, S. D.; Yao, Y. G.; Hu, L. B. Rapid, *in situ* synthesis of high capacity battery anodes through high temperature radiation-based thermal shock. *Nano Lett.* **2016**, *16*, 5553–5558.
- [52] Li, Y. J.; Chen, Y. N.; Nie, A. M.; Lu, A. J.; Jacob, R. J.; Gao, T. T.; Song, J. W.; Dai, J. Q.; Wan, J. Y.; Pastel, G. et al. *In situ*, fast, high-temperature synthesis of nickel nanoparticles in reduced graphene oxide matrix. *Adv. Energy Mater.* **2017**, *7*, 1601783.
- [53] Soler, J. M.; Artacho, E.; Gale, J. D.; García, A.; Junquera, J.; Ordejón, P.; Sánchez-Portal, D. The SIESTA method for *ab initio* order-*N* materials simulation. *J. Phys. Condens. Matter* **2002**, *14*, 2745–2779.
- [54] Dai, K.; Li, D. P.; Lu, L.; Liu, Q.; Lv, J. L.; Zhu, G. P. Facile synthesis of a reduced graphene oxide/cobalt sulfide hybrid and its electrochemical capacitance performance. *RSC Adv.* **2014**, *4*, 29216–29222.
- [55] Guo, D. H.; Shibuya, R.; Akiba, C.; Saji, S.; Kondo, T.; Nakamura, J. Active sites of nitrogen-doped carbon materials for oxygen reduction reaction clarified using model catalysts. *Science* **2016**, *351*, 361–365.
- [56] Wang, Z. Y.; Dong, Y. F.; Li, H. J.; Zhao, Z. B.; Wu, H. B.; Hao, C.; Liu, S. H.; Qiu, J. S.; Lou, X. W. Enhancing lithium-sulphur battery performance by strongly binding the discharge products on amino-functionalized reduced graphene oxide. *Nat. Commun.* **2014**, *5*, 5002.
- [57] Deng, J.; Ren, P. J.; Deng, D. H.; Bao, X. H. Enhanced electron penetration through an ultrathin graphene layer for highly efficient catalysis of the hydrogen evolution reaction. *Angew. Chem., Int. Ed.* **2015**, *54*, 2100–2104.
- [58] Wang, H. T.; Lee, H. W.; Deng, Y.; Lu, Z. Y.; Hsu, P. C.; Liu, Y. Y.; Lin, D. C.; Cui, Y. Bifunctional non-noble metal oxide nanoparticle electrocatalysts through lithium-induced conversion for overall water splitting. *Nat. Commun.* **2015**, *6*, 7261.
- [59] Xia, B. Y.; Yan, Y.; Li, N.; Wu, H. B.; Lou, X. W.; Wang, X. A metal-organic framework-derived bifunctional oxygen electrocatalyst. *Nat. Energy* **2016**, *1*, 15006.
- [60] Ledendecker, M.; Krick Calderón, S.; Papp, C.; Steinrück, H. P.; Antonietti,

- M.; Shalom, M. The synthesis of nanostructured Ni₅P₄ films and their use as a non-noble bifunctional electrocatalyst for full water splitting. *Angew. Chem., Int. Ed.* **2015**, *54*, 12361–12365.
- [61] Deng, J.; Ren, P. J.; Deng, D. H.; Yu, L.; Yang, F.; Bao, X. H. Highly active and durable non-precious-metal catalysts encapsulated in carbon nanotubes for hydrogen evolution reaction. *Energy Environ. Sci.* **2014**, *7*, 1919–1923.
- [62] Morales-Guio, C. G.; Stern, L. A.; Hu, X. L. Nanostructured hydrotreating catalysts for electrochemical hydrogen evolution. *Chem. Soc. Rev.* **2014**, *43*, 6555–6569.
- [63] Zheng, Y.; Jiao, Y.; Zhu, Y. H.; Li, L. H.; Han, Y.; Chen, Y.; Du, A. J.; Jaroniec, M.; Qiao, S. Z. Hydrogen evolution by a metal-free electrocatalyst. *Nat. Commun.* **2014**, *5*, 3783.
- [64] de Chialvo, M. R. G.; Chialvo, A. C. Hydrogen evolution reaction: Analysis of the Volmer-Heyrovsky-Tafel mechanism with a generalized adsorption model. *J. Electroanal. Chem.* **1994**, *372*, 209–223.
- [65] Zheng, Y.; Jiao, Y.; Jaroniec, M.; Qiao, S. Z. Advancing the electrochemistry of the hydrogen-evolution reaction through combining experiment and theory. *Angew. Chem., Int. Ed.* **2015**, *54*, 52–65.
- [66] Hammer, B.; Nørskov, J. K. Theoretical surface science and catalysis—calculations and concepts. *Adv. Catal.* **2000**, *45*, 71–129.
- [67] Nørskov, J. K.; Bligaard, T.; Logadottir, A.; Kitchin, J. R.; Chen, J. G.; Pandelov, S.; Stimming, U. Trends in the exchange current for hydrogen evolution. *J. Electrochem. Soc.* **2005**, *152*, J23–J26.
- [68] Hammer, B.; Nørskov, J. K. Why gold is the noblest of all the metals. *Nature* **1995**, *376*, 238–240.

Electronic Supplementary Material

Millisecond synthesis of CoS nanoparticles for highly efficient overall water splitting

Yanan Chen^{1,§}, Shaomao Xu^{1,§}, Shuze Zhu^{2,§}, Rohit Jiji Jacob³, Glenn Pastel¹, Yanbin Wang¹, Yiju Li¹, Jiaqi Dai¹, Fengjuan Chen¹, Hua Xie¹, Boyang Liu¹, Yonggang Yao¹, Lourdes G. Salamanca-Riba¹, Michael R. Zachariah³, Teng Li², and Liangbing Hu¹ (✉)

¹ Department of Materials Science and Engineering, University of Maryland College Park, College Park, Maryland 20742, USA

² Department of Mechanical Engineering, University of Maryland College Park, College Park, Maryland 20742, USA

³ Department of Chemical and Biomolecular Engineering and Chemistry and Biochemistry, University of Maryland College Park, College Park, Maryland 20742, USA

[§] Yanan Chen, Shaomao Xu, and Shuze Zhu contributed equally to this work.

Supporting information to <https://doi.org/10.1007/s12274-019-2304-0>

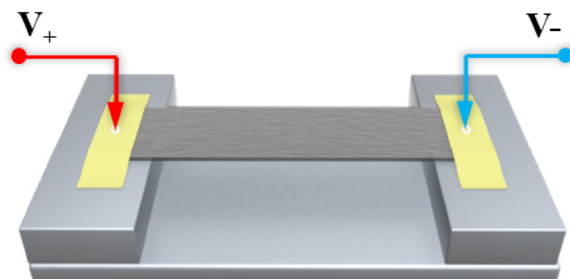


Figure S1 Home-made experimental setup for carrying out the thermal shock high temperature treatment by applying a current or voltage through the samples.

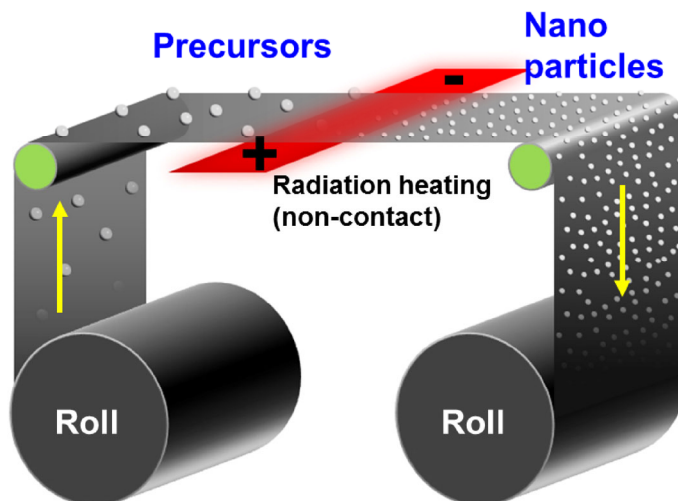


Figure S2 A schematic to show the nanoparticle roll-to-roll manufacturing process induced by thermal shock. As the film passes through the radiation heating zone at a suitable speed, the salts hosted in the RGO matrix are transformed into nanoparticles.

Address correspondence to binghu@umd.edu

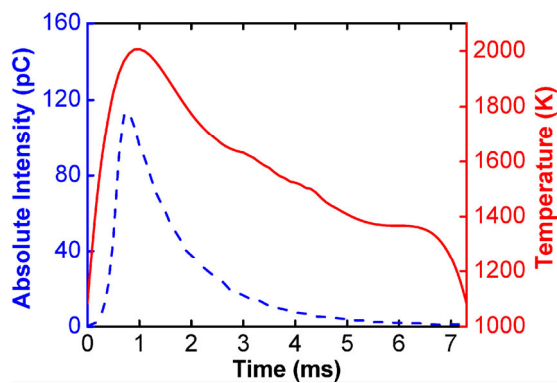


Figure S3 Intensity profile on the 853 nm channel accompanied with temperature in the ultra-fast synthesis process.

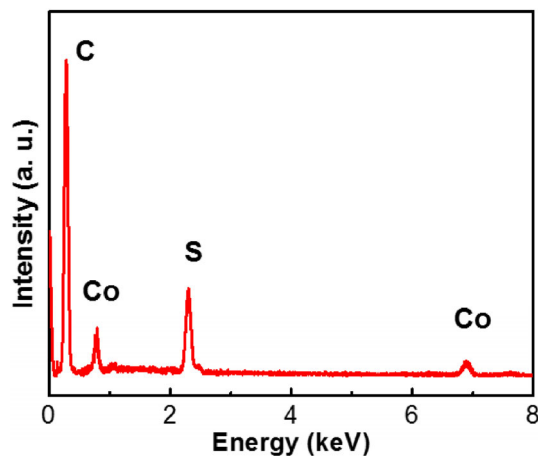


Figure S4 EDX spectra of cobalt-sulfide nanoparticle.

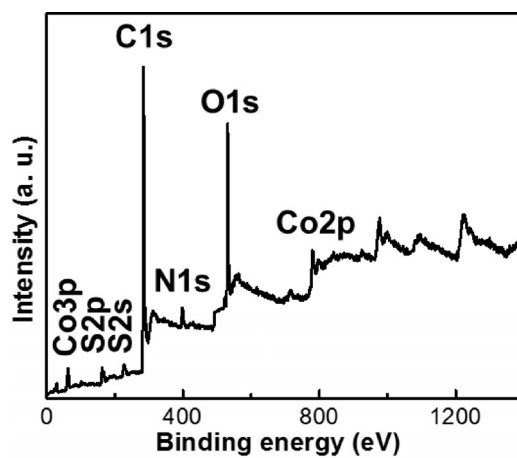


Figure S5 XPS survey spectra of CoS-RGO.

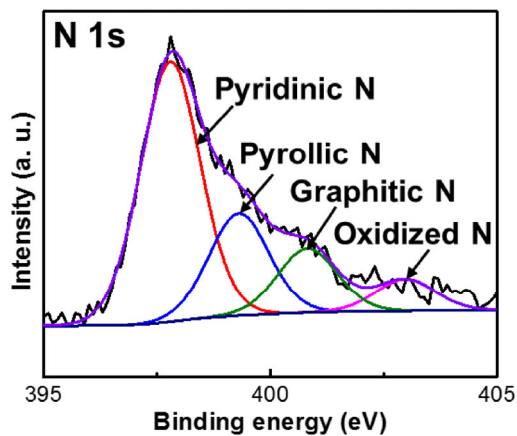


Figure S6 High-resolution N 1s XPS spectrum of CoS-RGO.

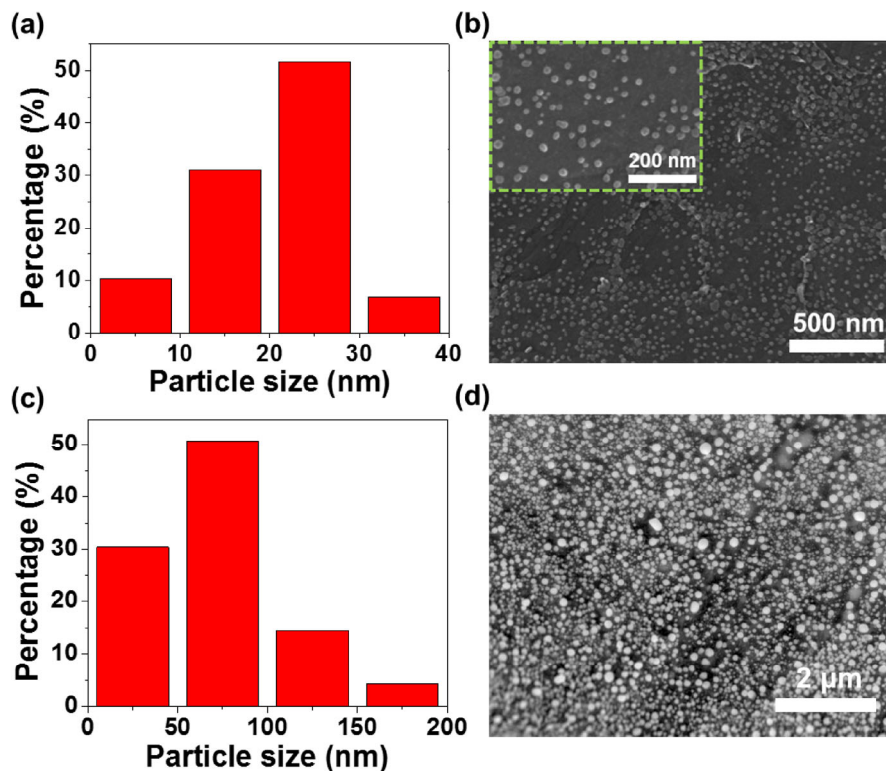


Figure S7 (a) and (b) Statistical particle size distribution and SEM image of CoS nanoparticles loaded on RGO after 7 ms thermal shock treatment. (c) and (d) Statistical particle size distribution and SEM image of CoS nanoparticles loaded on RGO after 5 min thermal shock treatment, which confirms the importance of the short duration in the synthesis of nanoparticles with a small size.

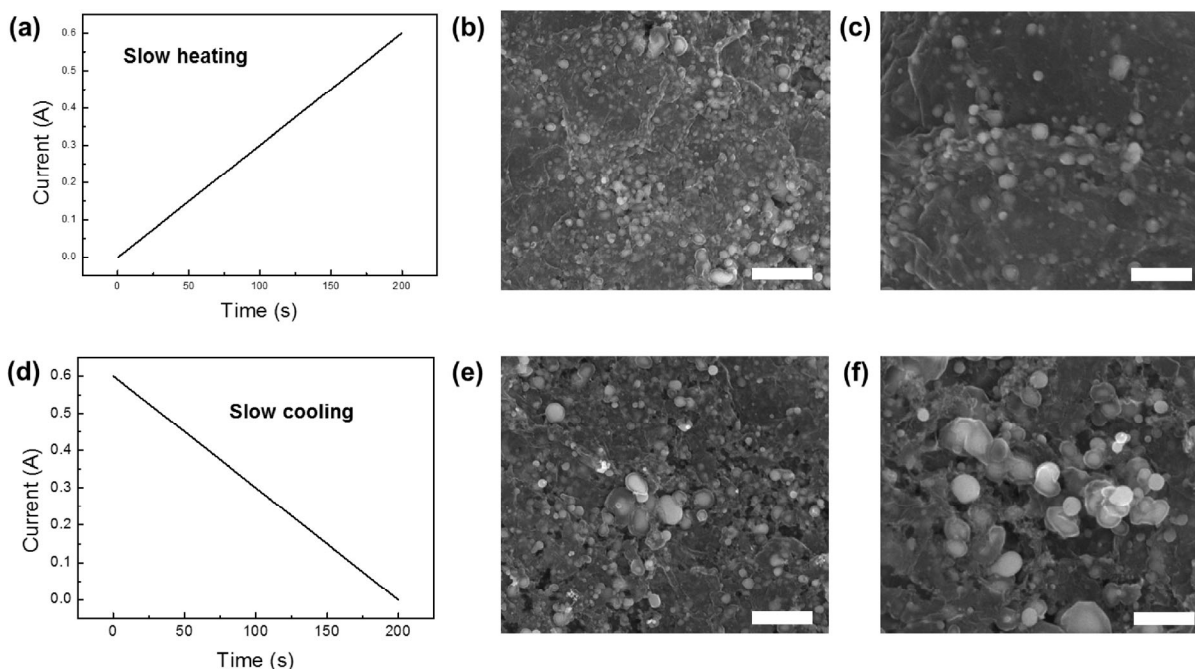


Figure S8 Nanoparticles synthesized by slow heating and cooling rates. (a)–(c) Slow heating profile (10 K/s) and SEM images of the resulting CoS nanoparticles. (d)–(f) Slow cooling profile (10 K/s) and SEM images of the resulting CoS nanoparticles. Scale bars, 1 μm (b, e), 500 nm (c, f).

Figures S10(a) and S10(b) shows the polarization curve and Tafel plot of the CoS-RGO electrocatalyst with a mass loading of 0.5 mg cm^{-2} in $0.5 \text{ M H}_2\text{SO}_4$ solution. The CoS-RGO exhibits excellent HER activity with the lowest onset overpotential of 0 mV versus reversible hydrogen electrode (RHE), approaching the performance of commercial 40 wt.% Pt/C and much higher than RGO decorated with Co nanoparticles or nitrogen and sulfur doped RGO, as shown in Figure S10a. Small overpotentials of 17 mV, 74 mV and 149 mV are required for the CoS-RGO electrocatalyst to reach -1 , -10 and -100 mA cm^{-2} cathodic currents, respectively, which are among the most active for non-noble material based electrocatalysts (Table S1). In contrast, N- and S-doped RGO need an applied potential of $\sim 540 \text{ mV}$ to achieve 10 mA cm^{-2} of cathodic current, and pure RGO film shows negligible activity in the measured voltage range, confirming that such high electrocatalytic performance mainly comes from the synthesized CoS nanoparticles. The corresponding Tafel plot, as depicted in Figure S10(b), shows a small Tafel slope of $\sim 56 \text{ mV dec}^{-1}$ for CoS-RGO, which is higher than 30.7 mV dec^{-1} for 40 wt.% Pt/C electrocatalyst, suggesting a

Volmer-Heyrovsky reaction mechanism. The exchange current density of the CoS-RGO electrocatalyst is obtained as $0.5035 \text{ mA cm}^{-2}$ by extrapolating the Tafel plot (Figure S11), which is larger than that of Pt/C with a value of 0.39 mA cm^{-2} . Furthermore, the catalyst exhibits a high turnover frequency (TOF) of 0.1 s^{-1} per active site at 149 mV overpotential (100 mA cm^{-2}), indicating the excellent intrinsic catalytic activity of the as-synthesized CoS-RGO electrocatalyst (Figure S12). Stability is always a critical aspect in catalyst evaluation for long-term application. To assess the durability of the CoS-RGO electrocatalyst in acidic conditions, accelerated linear potential sweeps were carried out continuously at a scan rate of 50 mV s^{-1} (Figure S10c). The polarization curve shows a negligible decay after 500 repeated potential sweeps, which implies that the catalyst is highly stable without any obvious corrosion. Furthermore, the stability of the electrocatalyst is evaluated by electrolysis at fixed potentials over prolonged periods. A stable current density of $\sim 20 \text{ mA cm}^{-2}$ was observed after 10 h testing at an overpotential of 120 mV (Figure S10(d)). The catalytic current exhibits little loss in the first 2 hours and then fully stabilizes for the rest of the electrolysis.

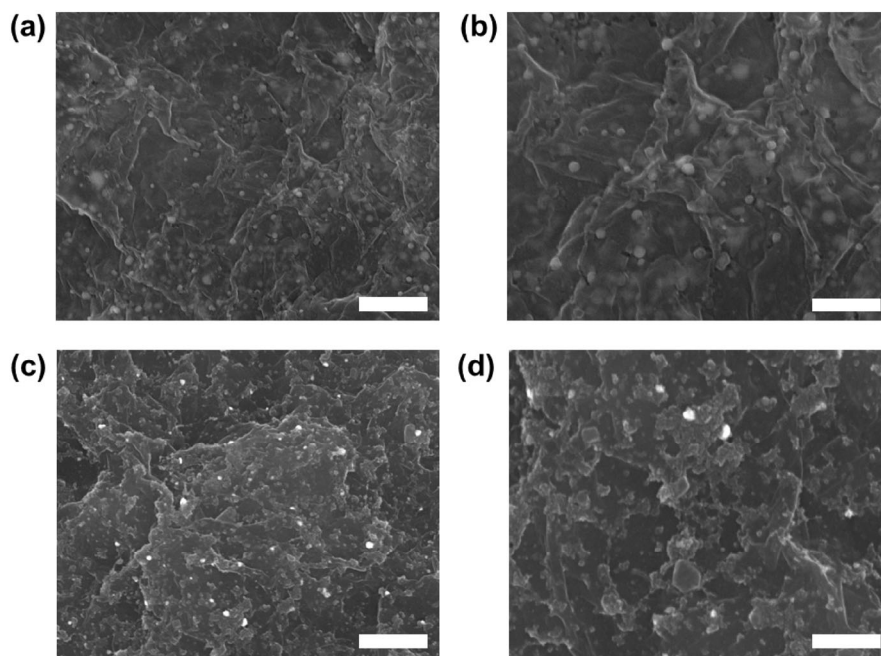


Figure S9 SEM images of the synthesized CoS nanoparticles by 7 ms thermal shock at 1500 K (a) and (b) and 1000 K (c) and (d). Scale bars, $1 \mu\text{m}$ (a, c), 500 nm (b, d). Compared with thermal shock at 2000 K, a lower thermal shock temperature leads to larger sized particles, which is probably due to the lack of sufficient energy to highly disperse the materials.

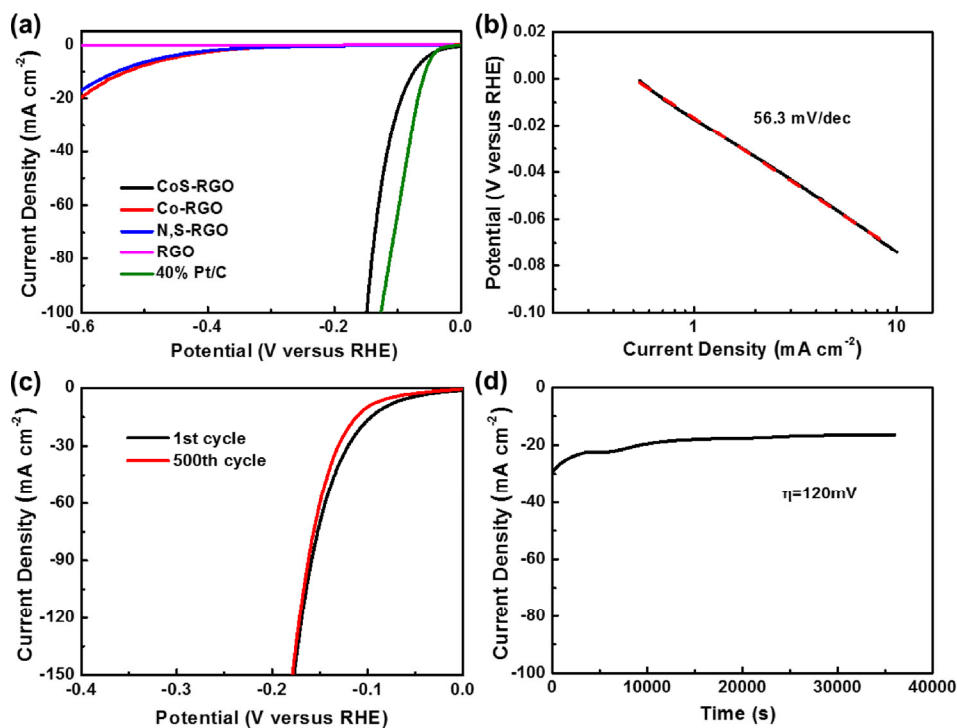


Figure S10 HER performance of CoS@ few-layer graphene core-shell nanoparticles. (a) The HER polarization curves of CoS-RGO compared with RGO, Co-RGO, N,S-RGO at 2 mV s^{-1} in $0.5 \text{ M H}_2\text{SO}_4$. (b) Tafel plot of CoS-RGO. (c) Polarization curves after continuous potential sweeps at 50 mV s^{-1} in $0.5 \text{ M H}_2\text{SO}_4$. (d) Time dependence of cathodic current density during electrolysis under $\eta = 120 \text{ mV}$ in $0.5 \text{ M H}_2\text{SO}_4$.

Table S1 Comparison of HER performance in acidic electrolytes for CoS-RGO with state-of-the-art cobalt chalcogenides.

Catalyst	Mass Loading mg cm ⁻²	Onset η (mV)	Tafel Slope (mV decade ⁻¹)	Current density (j, mA cm ⁻²)	η at corresponding j (mV)	Ref
CoS-RGO	0.5	0	56	10 100	74 149	This work
CoS ₂ /RGO-CNT	1.15	~100	51	10 100	142 178	1
CoS ₂	--	60	52	10	190	2
CoS ₂ nanowires	1.7	75	52	10	145	3
CoSe ₂ NP/CP	2.5	~90	42	10 100	137 181	4
CoS ₂	0.037	~100	44.6	4	220	5
Fe _{0.43} Co _{0.57} S ₂	0.037	~100	55.9	4	190	5
CoPS film		~50	57	10	128	6

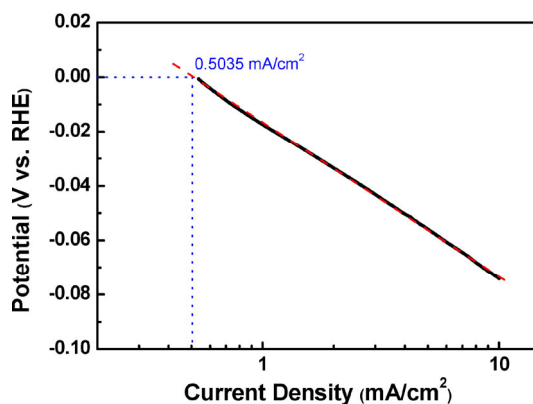


Figure S11 HER Tafel plot of CoS-RGO showing the extrapolation to zero overpotential. The exchange current density was determined to be 0.5035 mA/cm².

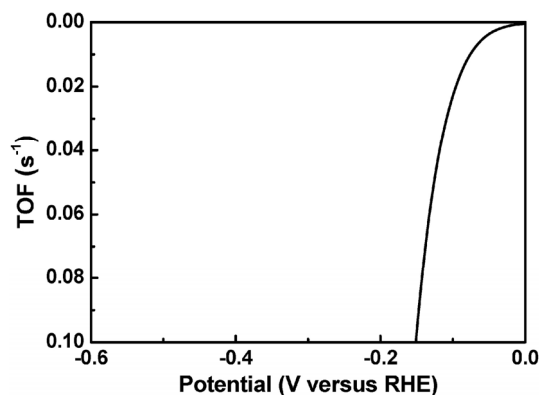


Figure S12 Turnover frequency (TOF) vs. potential in 0.5 M H₂SO₄. TOF = $jM/2Fm$, where j is the current density, F is Faraday's constant (96485.3 C mol⁻¹), M is the molar mass of CoS, m is the loading mass of CoS, and the number 2 refers to 2 electrons per mole of H₂. According to the inductively coupled plasma emission spectroscopy (ICP) result, the loading mass of CoS is 0.27 mg cm⁻² derived from the mass ratio of Co (35%).

Table S2 Comparison of OER performance in alkali electrolytes for CoS-RGO with state-of-the-art cobalt chalcogenides and non-noble metal based compounds.

Catalyst	Mass Loading mg cm ⁻²	Tafel Slope (mV decade ⁻¹)	Current density (j, mA cm ⁻²)	η at corresponding j (V)	Ref
CoS-RGO	0.5	71	10 100	1.58 1.66	This work
Co _{1-x} S	0.0926	55.6	10	1.6	7
CoP/NCNHP	2	--	10	1.54	8
Co-P/NC	1	52	10	1.55	9
FeNiO	4.12	77	10	1.52	10
CoMoS	2.23	81.3	10	~1.58	11
P-CoMoS	2.19	70.2	10	~1.5	11
N-WC	16	--	10	<1.55	12

Table S3 Comparison of overall water splitting performance in alkali electrolytes for CoS-RGO with state-of-the-art cobalt chalcogenides and non-noble metal based compounds.

Catalyst	Mass Loading mg cm ⁻²	Current density (j, mA cm ⁻²)	η at corresponding j (V)	Substrate	Ref
CoS-RGO	0.5	10 100	1.75 1.97	Free-standing	This work
N-WC	16	10	<1.5	Free-standing	12
CoP/NCNHP	2	10 100	1.64 ~1.9	Carbon paper	8
CoSe	3.8	10 100	1.65 ~1.9	Ti	13
NiFeOx/CNF	1.6 3	10 10	1.65 1.51	Free-standing	14
CoOx@CN	2	10	~1.6	Nickel foam	15
Fe _{0.43} Co _{0.57} S ₂	2.8	10	1.63	Nickel foam	16
MoS ₂ /Ni ₃ S ₂	9.7	10	1.56	Nickel foam	17
FeNiO	4.12	10	1.46	Nickel foam	10
P-CoMoS	2.19	10	1.54	Free-standing	11

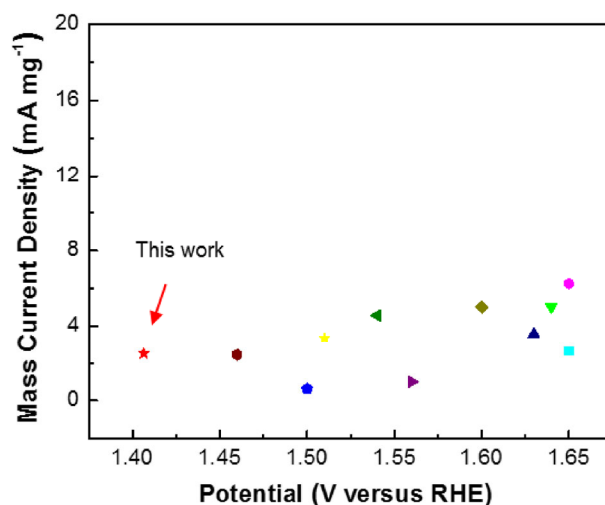


Figure S13 Mass current activity of CoS-RGO compared with state-of-the-art non-noble metal based compounds, indicating the high mass activity of the as-synthesized CoS-RGO catalyst.

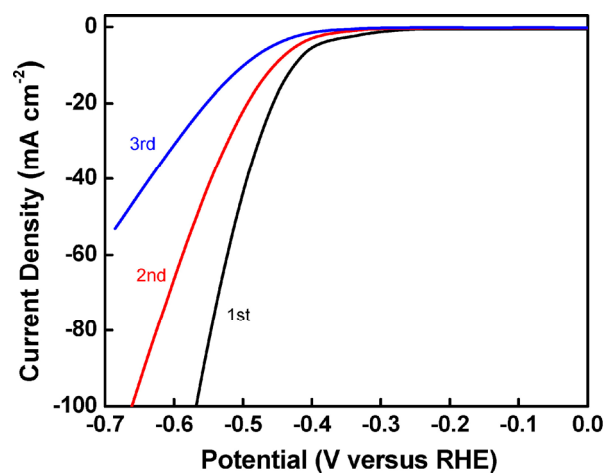


Figure S14 HER polarization curve of CoS without graphene. The catalytic activity decays drastically after only 3 cycles.

Figure S15 (a) shows the top view and side view of a CoS Crystal cell. OA, OB, OC are the cell axes. The length of OA is 0.3367 nm. The length of OB is 0.3367 nm. The length of OC is 0.516 nm. Lattice vector and atom coordinates are displayed as below.

Lattice Vector (Å)			
A=	3.367000000	0.000000000	0.000000000
B=	-1.683500000	2.915910000	0.000000000
C=	0.000000000	0.000000000	5.160000000
Coordinates (Å)			
S	0.000000000	1.9439383560	1.2900000000
S	1.683500000	0.9719691780	3.8700000000
Co	0.000000000	0.000000000	0.000000000
Co	0.000000000	0.000000000	2.580000000

The red line in (a) shows the cutting plane to create the surface as used in Figure S15(b) to S15d and main text Figure 6. Figure S15(b) shows the slab model presented in a unit cell from different viewing perspectives (these viewing perspectives also apply to the remaining of this supplementary information). The unit cell has the following geometrical size: a (along OA direction) = 2.3569 nm, b (along OB direction) = 0.3367 nm, c (along OC direction) = 0.516 nm; alpha = 90 degrees, beta = 90 degrees, gamma = 120 degrees. There are 9 water molecules filling up the vacuum space. The geometrical dimension of the vacuum space along OA direction is 1.6835 nm, giving a water density 1.0631 g/cm³. 1x7x5 Monkhorst-Pack k-points are used. Please note that all calculations are performed using the unit cell model but the presentation may be in a supercell for visual clarity as explained next. Figure S15(c) shows the slab model presented in a supercell. The grey box schematics shows the zoomed region for display in main text Figure 6. Similar definition of the zoomed view also applies to the remaining of this supplementary information.

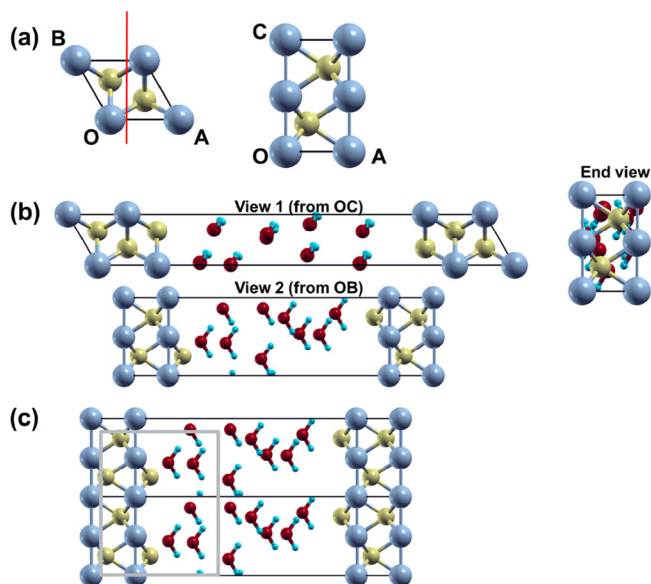


Figure S15 (a) An unit cell for the CoS crystal. The red line shows the cutting plane to create the slab model. (b) A slab model with three perspective views. This model is used for main text Figure 6. (c) The slab model presented in a supercell. The grey box schematics shows the zoomed region for display in main text Figure 6.

Figure S16 shows the multiple rounds of Volmer reactions on the surface as shown in Figure 6 in main text from two viewing perspectives in a zoomed view. Figure S16(a) shows that two pairs of protons and electrons (two additional hydrogen atoms) are added to the unit cell for the starting round of simulation. Two H are adsorbed on Co and S respectively. Figure S16(b) shows that, after adding a new pair of proton and electron (one additional hydrogen atom), we don't see the adsorption of the H on to the catalyst surface. Instead, we observe that the H that initially adsorbed on S has changed its adsorption site to Co. This also suggests that the H adsorbed on S is much more active than those adsorbed on Co. Figure S16(c) shows that, after adding a new pair of proton and electron (one additional hydrogen atom), a H is adsorbed on S. This is the last round of simulation before the production of hydrogen molecules occurs (see Figure 6 in main text) if further adding new pair of proton and electron.

Figure S17 shows geometry-optimized structures of the slab model, without water molecules filling the vacuum. These are the structures used for DOS calculations as in Figure 6. Moderate changes on the surface morphology upon hydrogen adsorption are seen. 10x70x50 k-points are used for calculating the DOS.

Note that we do not observe the apparent Tafel reaction, which requires two adsorbed hydrogen atoms. Since an S site usually can only accommodate one hydrogen atom, at least one of these two hydrogen atom has to be from these adsorbed on Co. The fact that the Co site is less active could possible hinder the Tafel reaction.

Figure S18(a) shows two other cutting planes to have only S or Co exposed for reaction. The slab models are created in a similarly way as shown in Figure S16. The unit cell of slab model has the following geometrical size: a (along OA direction) = 0.3367 nm, b (along OB direction) = 0.3367 nm, c (along OC direction) = 2.58 nm; alpha = 90 degrees, beta = 90 degrees, gamma = 120 degrees. There are 5 water molecules filling up the vacuum space. The geometrical dimension of the vacuum space along OA direction is 1.548 nm, giving a water

density 0.9843 g/cm³. 7x7x1 Monkhorst-Pack k-points are used. Figure S18b shows that after two rounds of AIMD simulations, the Co is hydrogenated with two H atoms. Figure S18(c) shows that further adding of H atom does not trigger the production of hydrogen molecule. The Co is still hydrogenated with two H atoms. Figure S18(d) shows that in a similar setup but using the S exposed surfaces, the HER could easily occur. The above also demonstrates that S is the active site. Figure S19 presents the DOS calculations on these two types of surfaces.

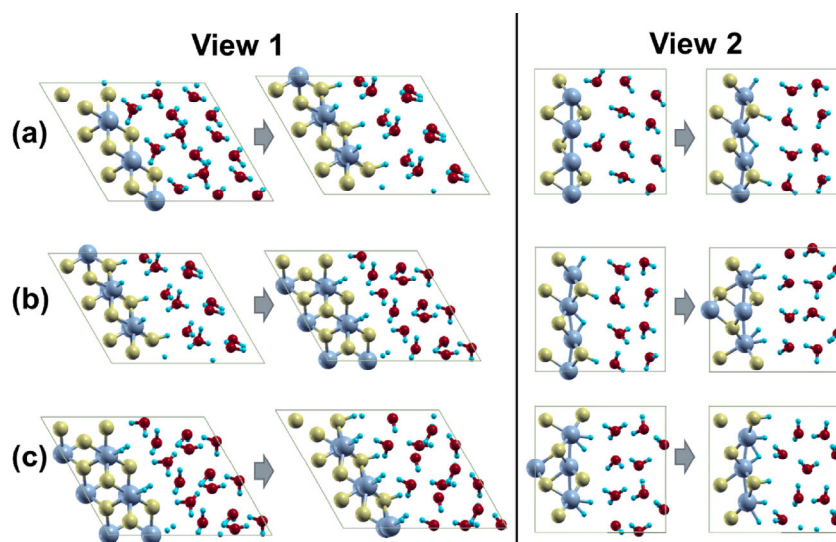


Figure S16 Multiple rounds of Volmer reactions on the surface as shown in Figure 6 in the main text from two viewing perspectives in a zoomed view.

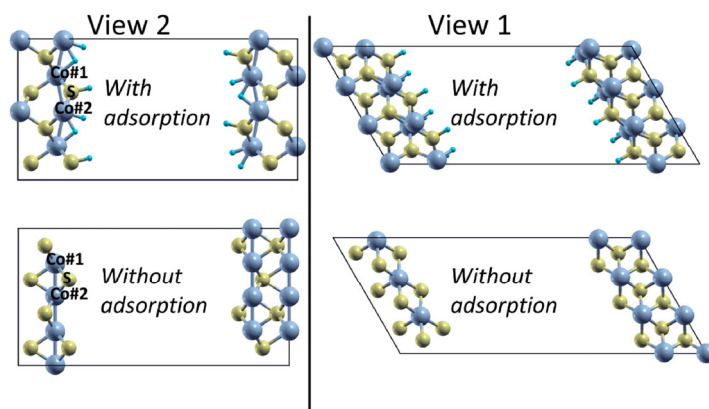


Figure S17 Geometry-optimized structures of the slab model without water, which are used for DOS calculation.

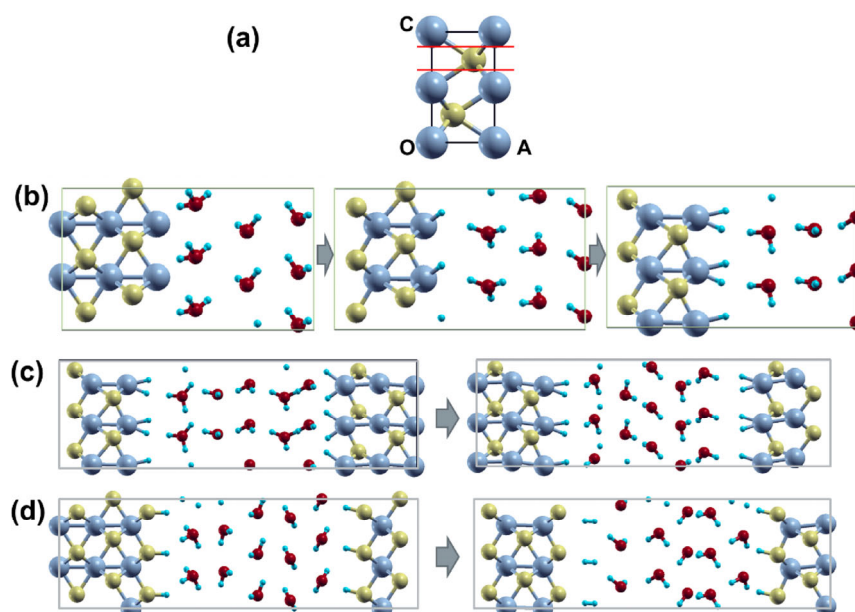


Figure S18 (a) Schematic showing the generation of new types of surfaces from CoS crystal. Red lines denote the cutting plane. (b) The Co is hydrogenated with two H atoms after two rounds of simulating Volmer reaction. (c) Further adding of H atom doesn't trigger the production of hydrogen molecule on Co exposed surface. (d) HER could easily occur on S exposed surfaces.

Figure S19(a) shows the DOS calculated for the Co exposed surface with and without hydrogen adsorption. The calculation is performed in a similar way as in Figure S17. 70x70x10 k-points are used for calculating the DOS. It shows that there is no apparent peak of anti-bonding states of Co emerging above the Fermi level upon hydrogen adsorption. On the contrary, Figure S19(b) shows that there is an apparent peak of anti-bonding states of Co emerging above the Fermi level upon hydrogen adsorption. This supports that S is a more active reaction site than Co.

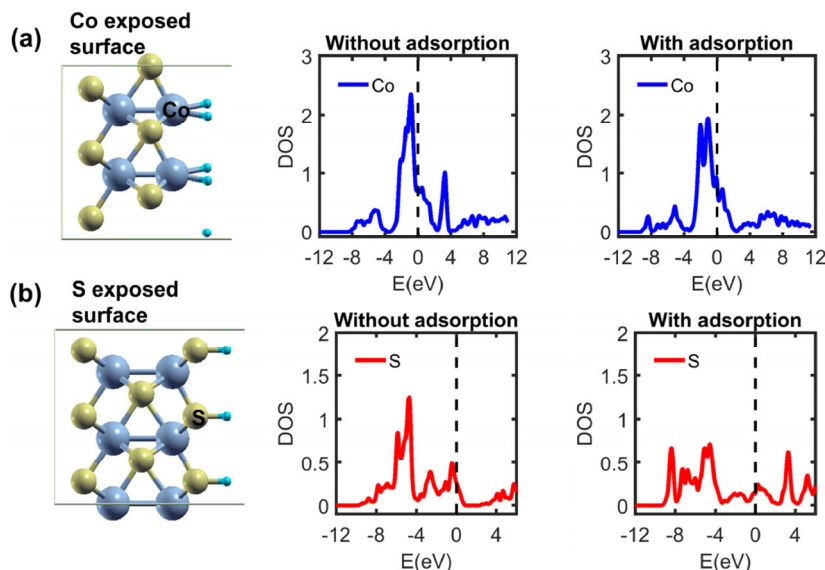


Figure S19 (a) DOS calculated for the Co exposed surface with and without hydrogen adsorption. (b) DOS calculated for the S exposed surface with and without hydrogen adsorption.

References

- [S1] Peng, S.; Li, L.; Han, X.; Sun, W.; Srinivasan, M.; Mhaisalkar, S. G.; Cheng, F.; Yan, Q.; Chen, J.; Ramakrishna, S. Cobalt Sulfide Nanosheet/graphene/carbon Nanotube Nanocomposites as Flexible Electrodes for Hydrogen Evolution. *Angew. Chem. Int. Ed Engl.* **2014**, *53*, 12594–12599.
- [S2] Faber, M. S.; Lukowski, M. A.; Ding, Q.; Kaiser, N. S.; Jin, S. Earth-Abundant Metal Pyrites (FeS₂, CoS₂, NiS₂, and Their Alloys) for Highly Efficient Hydrogen Evolution and Polysulfide Reduction Electrocatalysis. *J. Phys. Chem. C* **2014**, *118*, 21347–21356.
- [S3] Faber, M. S.; Dziedzic, R.; Lukowski, M. A.; Kaiser, N. S.; Ding, Q.; Jin, S. High-Performance Electrocatalysis Using Metallic Cobalt Pyrite (CoS₂) Micro- and Nanostructures. *J. Am. Chem. Soc.* **2014**, *136*, 10053–10061.
- [S4] Kong, D.; Wang, H.; Lu, Z.; Cui, Y. CoSe₂ Nanoparticles Grown on Carbon Fiber Paper: An Efficient and Stable Electrocatalyst for Hydrogen Evolution Reaction. *J. Am. Chem. Soc.* **2014**, *136*, 4897–4900.
- [S5] Kong, D.; Cha, J. J.; Wang, H.; Lee, H. R.; Cui, Y. First-Row Transition Metal Dichalcogenide Catalysts for Hydrogen Evolution Reaction. *Energy Environ. Sci.* **2013**, *6*, 3553–3558.
- [S6] Cabán-Acevedo, M.; Stone, M. L.; Schmidt, J. R.; Thomas, J. G.; Ding, Q.; Chang, H.-C.; Tsai, M.-L.; He, J.-H.; Jin, S. Efficient Hydrogen Evolution Catalysis Using Ternary Pyrite-Type Cobalt Phosphosulphide. *Nat. Mater.* **2015**, *14*, 1245–1251.
- [S7] Xu, Y.; Hao, Y.; Zhang, G.; Jin, X.; Wang, L.; Lu, Z.; Sun, X. One-Step Scalable Production of Co_{1-x}S/Graphene Nanocomposite as High-Performance Bifunctional Electrocatalyst. *Part. Part. Syst. Charact.* **2016**, *33*, 569–575.
- [S8] Pan, Y.; Sun, K.; Liu, S.; Cao, X.; Wu, K.; Cheong, W.-C.; Chen, Z.; Wang, Y.; Li, Y.; Liu, Y.; et al. Core-Shell ZIF-8@ZIF-67-Derived CoP Nanoparticle-Embedded N-Doped Carbon Nanotube Hollow Polyhedron for Efficient Overall Water Splitting. *J. Am. Chem. Soc.* **2018**, *140*, 2610–2618.
- [S9] You, B.; Jiang, N.; Sheng, M.; Gul, S.; Yano, J.; Sun, Y. High-Performance Overall Water Splitting Electrocatalysts Derived from Cobalt-Based Metal–Organic Frameworks. *Chem. Mater.* **2015**, *27*, 7636–7642.
- [S10] Qian, M.; Cui, S.; Jiang, D.; Zhang, L.; Du, P. Highly Efficient and Stable Water-Oxidation Electrocatalysis with a Very Low Overpotential Using FeNiP Substitutional-Solid-Solution Nanoplate Arrays. *Adv. Mater.* **2017**, *29*, 1704075.
- [S11] Ray, C.; Lee, S. C.; Sankar, K. V.; Jin, B.; Lee, J.; Park, J. H.; Jun, S. C. Amorphous Phosphorus-Incorporated Cobalt Molybdenum Sulfide on Carbon Cloth: An Efficient and Stable Electrocatalyst for Enhanced Overall Water Splitting over Entire pH Values. *ACS Appl. Mater. Interfaces* **2017**, *9*, 37739–37749.
- [S12] Han, N.; Yang, K. R.; Lu, Z.; Li, Y.; Xu, W.; Gao, T.; Cai, Z.; Zhang, Y.; Batista, V. S.; Liu, W.; et al. Nitrogen-Doped Tungsten Carbide Nanoarray as an Efficient Bifunctional Electrocatalyst for Water Splitting in Acid. *Nat. Commun.* **2018**, *9*, 924.
- [S13] Liu, T.; Liu, Q.; Asiri, A. M.; Luo, Y.; Sun, X. An Amorphous CoSe Film Behaves as an Active and Stable Full Water-Splitting Electrocatalyst under Strongly Alkaline Conditions. *Chem. Commun.* **2015**, *51*, 16683–16686.
- [S14] Wang, H.; Lee, H.-W.; Deng, Y.; Lu, Z.; Hsu, P.-C.; Liu, Y.; Lin, D.; Cui, Y. Bifunctional Non-Noble Metal Oxide Nanoparticle Electrocatalysts through Lithium-Induced Conversion for Overall Water Splitting. *Nat. Commun.* **2015**, *6*, 7261.
- [S15] Jin, H.; Wang, J.; Su, D.; Wei, Z.; Pang, Z.; Wang, Y. In Situ Cobalt–Cobalt Oxide/N-Doped Carbon Hybrids As Superior Bifunctional Electrocatalysts for Hydrogen and Oxygen Evolution. *J. Am. Chem. Soc.* **2015**, *137*, 2688–2694.
- [S16] Tang, C.; Cheng, N.; Pu, Z.; Xing, W.; Sun, X. NiSe Nanowire Film Supported on Nickel Foam: An Efficient and Stable 3D Bifunctional Electrode for Full Water Splitting. *Angew. Chem. Int. Ed.* **2015**, *54*, 9351–9355.
- [S17] Zhang, J.; Wang, T.; Pohl, D.; Rellinghaus, B.; Dong, R.; Liu, S.; Zhuang, X.; Feng, X. Interface Engineering of MoS₂/Ni₃S₂ Heterostructures for Highly Enhanced Electrochemical Overall-Water-Splitting Activity. *Angew. Chem. Int. Ed.* **2016**, *55*, 6702–6707.